Eng. Sci., 2023, **23**, 890

Engineered Science

DOI: https://dx.doi.org/10.30919/es890

Conducting Polymer/Hydrogel Hybrid Free-Standing Electrodes for Flexible Supercapacitors Capable of Self-Sensing Working Conditions: Large-Scale Fabrication Through Facile and Low-Cost Route

Madari Palliyalil Sidheekha,[1] Aranhikundan Shabeeba,[1] Lijin Rajan,[1] Mohamed Shahin Thayyil[2] and Yahya A. Ismail[1,*]

Abstract

Search for energy storage devices towards sustainability, compatibility and versatility demands flexible supercapacitors capable of sensing their surrounding conditions. Here, highly electroactive polyaniline/chitosan-hydrogel hybrid films were fabricated to develop a self-sensing motor. The hybrid electrodes showed remarkable supercapacitive properties with high-rate performance while capable of sensing electrical, thermal and chemical working conditions as evinced from the chronopotentiometric responses with consumed electrical energy as the sensing parameter. A single faradaic electrochemical reaction (the reversible oxidation-reduction) is responsible for both the sensing and charge storage properties of the hybrid film, which is exploited to develop a truly integrated sensing supercapacitor without additional connectivities. As a proof-of-concept, an all-solid-state symmetric supercapacitor was fabricated which showed large capacitance (111 mF cm^{-2} at 0.4 mA cm^{-2}), high energy density (13.8 µWh cm^{-2} at a power density of 100 µW cm^{-2}) as well as 74% capacitance retention after 5000 charge-discharge cycles. Besides, the current sensing characteristics of the device were tested from charge-discharge responses at a constant charged state to prove the above concept. This fundamental study provides a new direction for the development of simple and compatible self-sensing motors.

Keywords: Conducting polymer; Polyaniline; Hydrogel; Sensing supercapacitor; Electrochemical sensor; Sensing motors.
Received: 12 January 2023; Revised: 10 May 2023; Accepted: 13 May 2023.
Article type: Research article.

1. Introduction

With the rapid development of technology, designing novel multi-sensing devices (motors), especially capable of sensing and responding to changes in the working and surrounding environment is highly desired for developing intelligent and compatible devices. Until now, such systems are created by simply assembling each monofunctional device to form a unit to realize functional integration, which has complex manufacturing processes, increased overall size and reduced flexibility, which may limit the applications in lightweight flexible gadgets. Therefore, developing self-sensing devices using a single active material is of crucial practical significance which stimulates the development of smart and compatible devices in future electronics.

From the viewpoint of materials, conducting polymers (CPs) are one of the promising materials for developing soft motors for different applications. During oxidation/reduction, there is a change in the distribution of the sigma and pi bond along the CP chain. It induces conformational movement of the polymeric chain leading to de-coiling/coiling of the polymer chain and resulting in swelling/shrinking of the material. This process is reversible during reversible electrochemical reactions. Usually, the oxidation/reduction takes place in 'n' consecutive steps, each step involving one electron transfer. Therefore, the CP chain is regarded as a multi-step molecular motor.[1] CPs are also considered as 'multifunctional materials'; the different properties such as conductivity, volume, color, stored ion or stored charge change in a reversible and controlled way during the same reversible electrochemical reaction (reaction multifunctionality).[1] These property changes are effectively employed in the fabrication of various electrochemical devices and products:

---

[1] *Advanced Materials Research Center, Department of Chemistry, University of Calicut, Thenhipalam, Kerala - 673635, India.*

[2] *Department of Physics, University of Calicut, Thenhipalam, Kerala - 673635, India.*

*Email: aiyahya@uoc.ac.in (Y. I. Ismail)

supercapacitors,[2] actuators,[3,4] sensors,[5-7] light-emitting diodes[8-10] polymeric batteries[11,12] desalination,[13] smart drug delivery devices,[14] electrochromic windows[15,16] *etc*. At the same instant, different reaction properties, such as rate of reaction, potential evolution, consumed energy or charge during the reaction, adapt to or sense instantaneously the ambient mechanical, chemical, electrical or thermal working conditions (Otero's principle).[17,18] Our group is actively involved in the study of the reaction driven sensing properties of macromolecular motors (polymer chain) using different CPs such as polypyrrole, polyaniline, polyindole and poly-o-toluidine and establishing the fact that, this faradaic reaction driven sensing capability is a general property of all CPs.[19-23] Integrating this sensing principle of CPs with an electrochemical device (device working based on the electrochemical reaction of CPs) opens a new world of sensing motors (sensing supercapacitors, sensing actuators or sensing artificial muscle, sensing batteries, sensing membrane, sensing electrochemical transduces, *etc*.) responding to their working or surroundings condition through the same two connectivity. That is, CP offers full integration of sensing properties in a single device without additional connecting wires (same two connectivity for sensing and working signal) due to their unique electrochemical reactions: self-sensing motors.

The literature shows that CPs can be used for developing multifunctional devices. For example, Otero and co-workers demonstrated the concurrent sensing-actuators based on CPs; revealing that these motors can sense the temperature, electrolyte concentration, mechanical load on the actuator and flowing current, simultaneously, while working and proposed a physicochemical self-consistent model for describing quantitatively the dual sensing-actuating behaviors.[4,24-27] Here, only two connecting wires are required, which contain both sensing and actuation magnitudes. In addition, the charge stored during the oxidation/reduction reaction of CPs favors the development of batteries and supercapacitors (faradaic capacitors).[11,28,29] So, we are searching for the possibility of integrating the reaction driven sensing capabilities of CPs with charge storage capability to develop self-sensing supercapacitors, because, the demonstration of self-sensing properties in supercapacitor devices has not been explored so far.

The major challenges experienced by CPs in developing electrochemical devices for practical applications are their poor mechanical strength and lack of processability as well as the less electrochemical cycling stability as a consequence of the structural degradation caused by repeated swelling/shrinking during oxidation/reduction of polymer chains. Various strategies have been proposed by researchers to overcome these drawbacks: derivatization of the polymer backbone; co-polymerization with substituted monomers and introduction of lengthy substituent groups, sulfonic acid groups or carboxyl groups into the main chain;[30-35] the preparation of composites/hybrid/blend with processable polymers;[36-40] the use of surfactants;[41] composite/hybrid with metallic nanoparticles, graphene, carbon nanotubes and metal organic framework[42-44] or using polymeric/hydrogel nanofibers and microfibers as templates.[45-49] In literature, the development of composite/hybrid materials is a widely used strategy to improve the performance of electrochemical devices.[50-53] In this work, hybrid films were fabricated by adopting a facile and low-cost strategy suitable for large-scale production by the incorporation of polyaniline in a biocompatible hydrogel (Chitosan) in view of developing mechanically stable electrode materials.

Herein, we explore the simultaneous change of properties of CPs driven by oxidation/reduction reactions, as mentioned above, for developing a self-sensing motor, here it is a self-sensing supercapacitive device. As a conceptual exhibition, the multi-sensing supercapacitor is realized by Chitosan/polyaniline hybrid films (CPF), which can be very easily fabricated on a large scale, to perform as a supercapacitor electrode and sensor of working conditions such as electrical, thermal and chemical conditions. Here, the sensing of the working and surrounding environment through chronopotentiometric (charging-discharging) signals of the supercapacitor are demonstrated. It is a more attractive approach that truly integrates sensing and power. This research provides a valuable idea for designing energy storage devices capable to sense working and surrounding conditions during functioning.

2. Experimental

2.1 Materials

Chitosan (Cs) with a molecular weight of about 310000-375000 Da (Sigma Aldrich, USA) was used as received. AR Aniline (Merck Specialities, Pvt. Ltd, India) was distilled under a vacuum before use and stored in an inert atmosphere of less than 10 °C. Ammonium persulphate (APS), sodium hydroxide (NaOH), glacial acetic acid, sulphuric acid (H_2SO_4) and hydrochloric acid (HCl) (Merck Specialities, Pvt. Ltd, India) were directly taken and throughout the experiment, double distilled water was employed for washing of film and solution making.

2.2 Chitosan/polyaniline hybrid film preparation

The solution casting method was employed for preparing chitosan film. At first, chitosan powder was dissolved in 2% (w/v) acetic acid solution at room temperature to obtain a 1% (w/v) solution of chitosan and poured into a square glass plate (20 × 20 cm) and dried in the oven at 50 °C for 48 h. Then, peeled off the film and soaked in 1 M NaOH solution for 12 h to neutralize the film, thereby removing the acetate ions (CH_3COO^-) from the films. Then, thoroughly washed with distilled water and methanol several times to remove excess NaOH and dried at room temperature.

The chitosan/polyaniline films (CPF) were fabricated through an in situ chemical polymerization of aniline using

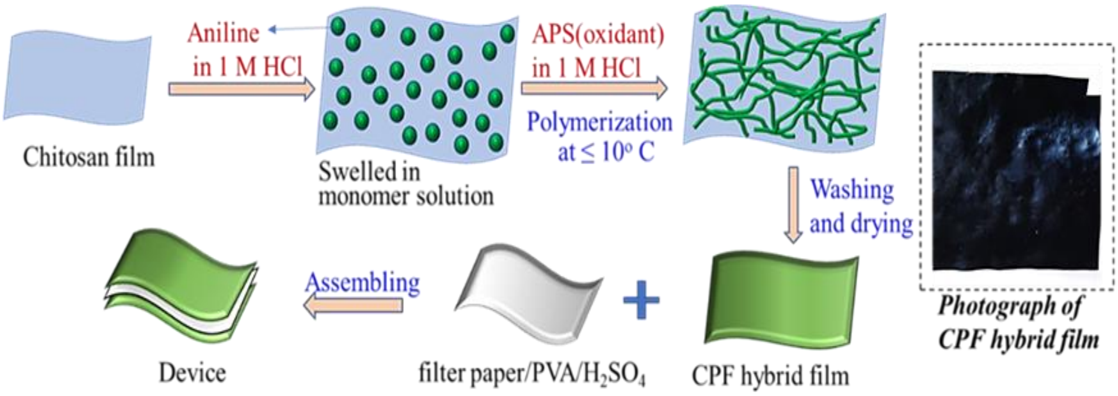

Fig. 1 Schematic representation of fabrication of CPF hybrid film and polymer supercapacitor device (the photograph of the hybrid film given on the right side).

ammonium persulfate as an oxidant in 1M aqueous HCl solution as depicted in Fig. 1. In brief, the chitosan film was immersed in a solution of 0.01 mole aniline in 100 mL of 1 M HCl solution for a period of 2 h. Then, added a solution of 0.0125 mole APS in 100 mL of 1 M HCl slowly with gentle shaking, after that, the reaction mixture was maintained at 10±2 °C for 24 h. The film was then washed thoroughly with a 1:1 methanol-distilled water mixture and dried at room temperature. The whole procedure was repeated to get high polyaniline content in the hybrid film. Here, hybrid films of up to four times of coating of polyaniline were fabricated and named as CPF1, CPF2, CPF3 and CPF4, respectively. This method is easy, inexpensive and suitable for large-scale fabrication of various conducting polymer/hydrogel hybrid films (Fig. S1 is the photograph of the fabricated film).

2.3 Fabrication of supercapacitor device

The all-solid-state symmetric supercapacitor device was fabricated by sandwiching two CPF4 films with filter paper/PVA/H_2SO_4 electrolyte layer as represented in Fig. 1. Typically, 20 mL of deionized water, 2 g H_2SO_4 and 2 g PVA were mixed at 80 °C with constant stirring until the mixture becomes transparent. A piece of filter paper was dipped in this electrolyte and allowed to dry until the excess water evaporated. Then, the two CPF hybrid films of 10 mm × 15 mm were stacked and pressed together with PVA/H_2SO_4 solid electrolyte in a filter paper as the middle layer to assemble a symmetric supercapacitor.

2.4 Characterizations

JASCO-4700 Spectrophotometer was used for Fourier transform infrared (FTIR) spectra (ATR mode) of all the samples in the range of 400-4000 cm^{-1}. WITEC ALPHA300 RA confocal Raman microscope with AFM with excitation at 533 nm was used for recording Raman spectra. The XRD patterns are obtained using PANalytical X'pert^3 diffractometer. Gemini SEM 300 field emission scanning electron microscope operated at an accelerating voltage of 5 kV was employed for surface morphology analysis and Energy Dispersive X-ray (EDX) spectral measurement using Gemini 300/EDS attached with the SEM was employed for the elemental analysis of the films. The electrical characterization was done using a Novocontrol BDS concept 80 Broadband Dielectric Spectrometer in a frequency range of 10^0-10^7 Hz at room temperature measured by sandwiching the film in between a couple of cylindrical gold-plated copper electrodes of the effective diameter of 30 mm and mounted between four probe electrodes of the BDS1200 sample cell. The DC electrical conductivities are obtained from frequency-dependent AC conductivity plots through fitting with Jonscher's power law ($\sigma_{a.c} = \sigma_{d.c} + A\omega^S$, where, ω is the angular frequency, A and s are the constant, usually $0 < s > 1$).[54-56] Shimadzu AGX-PLUS-10 kN universal test frame machine operated with a crosshead speed of 5 mm/min was used to study the mechanical characteristics of all the films. Young's modulus of the films was determined based on the secant modulus at the tensile strain of 2% since the elastic region of the stress-strain curve of CPF films was not linear.

All the electrochemical characterization, sensing and supercapacitive studies of hybrid films carried out by cyclic voltammetry (CV), galvanostatic charge-discharge (GCD) or chronopotentiometry and electrochemical impedance spectra (EIS) were performed using a Zahner Zennium Pro electrochemical galvanostat-potentiostat workstation attached to a personal computer and assisted with Thales XT electrochemical software. The electrochemical experiments using the CPF electrodes were carried out in a three-electrode cell with 2 × 10 mm hybrid film attached to the platinum wire with conductive carbon paste employed as working electrodes, an Ag/AgCl (3M KCl) electrode as a reference electrode, Pt wire as a counter electrode and aqueous HCl as the electrolyte. CV and GCD were recorded between -0.15 V and 0.80 V. The EIS spectra were recorded at an open-circuit voltage (OCV) with an amplitude of 10 mV in the frequency range from 1 Hz to 100 kHz at room temperature. The specific areal capacitance of the hybrid electrode and device was examined by CV and GCD. From the CV curve, the areal specific capacitance was calculated with the Eq. (1):

$$Cs = \frac{\int_{V_1}^{V_2} IdV}{Av(V_2 - V_1)} \tag{1}$$

where the integral signifies the total area under the CV curve recorded between the potential of V_1 and V_2, 'v' is the scan rate, and 'A' is the total area of the electrode in contact with the electrolyte or the total area of the device. From the GCD curves, the areal specific capacitance was obtained according to the Eq. (2):

$$\mathrm{Cs} = \frac{\mathrm{I}\Delta \mathrm{t}}{\mathrm{A}\Delta \mathrm{V}} \tag{2}$$

''I' denotes the discharging current and Δt represents the time lapse for discharging in seconds through the potential interval of ΔV (V_2- V_1) in volts. The areal energy density (E) and power density (P) of the supercapacitor device are calculated using the equations Eq. (3) and Eq. (4), respectively.

$$\mathrm{E} = \frac{\mathrm{C_s} * \Delta \mathrm{V}^2}{2 * 3600} \tag{3}$$

$$\mathrm{P} = \frac{3600\mathrm{E}}{\Delta \mathrm{t}} \tag{4}$$

3. Results and discussion

3.1 General characterizations

The FTIR spectra recorded for Cs, PANI, and CPF films in the range of 2000-500 cm^{-1} are presented in Fig. 2a. In the spectrum of Ch, the peak at 1645 cm^{-1} corresponds to C=O stretching and corroborates the presence of N-acetyl groups. The peaks at 1025, 1309 and 1564 cm^{-1} are assigned to C-O stretching, C-N stretching and N-H bending (amide II), respectively. The peak corresponding to C-H stretching vibrations appeared at 2888 cm^{-1} as well as the broad band in the region 3200–3600 cm^{-1} ascribed to O-H and N-H stretching vibrations, the broadness refers to the existence of intramolecular hydrogen bonds in the chitosan film. The FTIR spectrum of PANI exhibits a typical absorption peak corresponding to C=C stretching vibrations of benzenoid and quinoid rings at 1484 and 1560 cm^{-1} respectively, which denotes the PANI formed in emeraldine form. The absorption peaks at 1299 and 1248 cm^{-1} are ascribed to C-N stretching vibrations of the benzenoid–quinoid–benzenoid sequence as well as an intense peak around 1120 cm^{-1} is attributed to the charged defects.[57] FTIR spectra of CPF hybrid films have characteristic peaks of both PANI and chitosan with slight variations indicating the existence of interaction between them. All the films have two characteristic peaks corresponding to the stretching vibrations of C=C bonds of quinoid and benzenoid units of polyaniline in the region 1460-1570 cm^{-1} as noticed in the PANI. The bands around 1280 cm^{-1} and 1100 cm^{-1} are corresponding to the C-N stretching vibration of the secondary aromatic amine and C-H in-plane bending vibration of the benzene ring respectively. Besides, the appearance of a broad peak around the region 3200 - 3600 cm^{-1} is due to the overlapping of the N-H stretching of PANI with the O-H stretching of chitosan and indicates the hydrogen bonding interaction between chitosan and PANI.[58]

Figure 2b represents the Raman spectra of CPF films (For a better understanding, the Raman spectrum of the PANI is also added in the figure). The two characteristic bands observed were around 1340 cm^{-1} and 1570 cm^{-1} for all the hybrid films. The peak around 1340 cm^{-1} is ascribed to the vibration mode of the C-N^+ delocalized polaronic structure, which is characteristic of the protonated form of PANI and the peak around 1570 cm^{-1} is attributed to the C-C stretching of the benzenoid ring. It also confirms the formation of protonated (conductive) PANI through the chitosan matrix.[59] The XRD patterns for Cs, PANI, and CPF films are presented in Fig. 2c. For chitosan, characteristic diffraction peaks at 2θ = 9.9º and 19.8º attributed to hydroxyl and amine groups present in the chitosan structure. PANI shows the band at 2θ = 8.8º, 14.8º, 20.5º, and 25.2º, representing the polycrystalline nature of PANI. The peaks at 2θ = 20.5º, and 25.2 are due to parallel and perpendicular periodicity of the polymer chain of PANI. The diffraction pattern of CPF films has characteristic peaks of both chitosan and PANI with a small shift in the peak positions confirming the successful formation of stable hybrid films. The well-known peaks of chitosan at 9.9º and 19.8º have been shifted to around 18.5º and 11.5º, respectively in all CPF films. It is due to the overlapping of these peaks with peaks of PANI at 8.6º and 20.5º. Correspondingly PANI peaks are shifted to 8.3 and 23.4. This is also confirming the hybrid film formation.[60]

Figure 2d represents the frequency-dependent electrical conductivities of the hybrid films obtained in the frequency range of 10^{-2} to 10^{7} Hz measured using a broadband dielectric spectrometer. The frequency-dependent conductivity of CPF films follows power-law behavior indicative of hopping mechanisms. The CPF hybrid films exhibit good electrical characteristics though it is obtained from non-conducting chitosan which provides evidence for the homogeneous distribution of PANI inside as well as on the surface of chitosan film. The experimental data are fitted by Jonscher's universal power law to obtain the conductivity of hybrid films. The electrical conductivity of CPF1, CPF2, CPF3 and CPF4 is observed to be 3.15×10^{-4}, 2.79×10^{-3}, 6.04×10^{-2} and 4.34×10^{-1} S cm^{-1} respectively. The electrical conductivity of hybrid films is improved significantly with increasing PANI content in the film, *i.e.*, from CPF1 to CPF4. The high electrical conductivity of CPF hybrid film, fabricated by in situ chemical polymerization aniline on hydrogel (chitosan) film, suggests that our fabrication method can be utilized in realizing high electroactive hydrogel-based materials.

Mechanical characteristics of the CPF hybrid films were analyzed from linear stress-strain relations. The representative stress-strain curves of all four CPF films obtained at a crosshead rate of 50 mm/min are depicted in Fig. 2e and the results are listed in Table S1. The stress-strain curves of CPF films show plastic behavior. The literature shows that pure PANI film, generally obtained through electrochemical methods, is highly brittle and has very poor mechanical properties which limit its application as a free-standing electrode. However, the mechanical properties of the CPF hybrid film are good enough to be employed as an electrode material for electrochemical applications. The tensile strength and Young's Modulus of CPF4 films are 5.84 MPa and 1.56

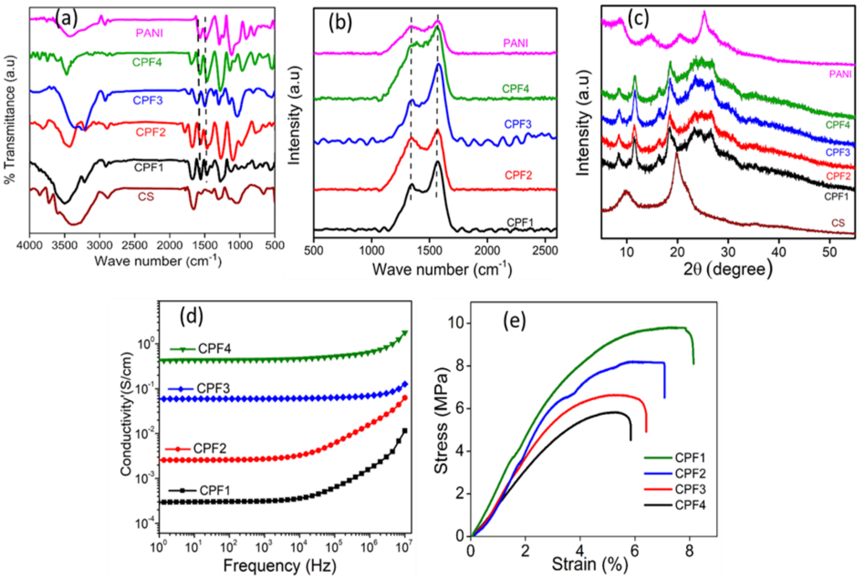

Fig. 2 (a) The FTIR spectra of chitosan, PANI and CPF films, (b) Raman spectra of CPF films (c) XRD patterns of chitosan, PANI, CPF films (d) frequency dependence conductivity of CPF films and (c) tensile stress-strain curve of CPF films.

MPa respectively. So, the method adopted here is useful for large-scale fabrication of conducting polymer-based stable and flexible free-standing electrode materials with good electrical as well as electrochemical properties. The tensile strength and Young's Modulus of the hybrid film decrease from CPF1 to CPF4. This may be related to the decrease in the degree of hydrogen bonding by the interpenetration of PANI chains through a highly hydrogen bonded chitosan film matrix. The maximum percentage elongation at break also decreases from CPF1 to CPF4, indicating that the stiffness of the film increases with the incorporation of more PANI into the chitosan matrix.

The surface morphology of films was investigated by FESEM analysis and the images are presented in Fig. 3. The SEM images reveal that the surface of chitosan film is quite smooth without voids or cracks (Fig. 3a) and the polyaniline grown on the chitosan matrix with coral-like nanowire structures during in situ chemical polymerization of aniline (Figs. 3b-e). Upon repeated coating, the new polyaniline has grown on the previously formed nanostructure leading to more agglomerated morphology on the higher coated states. The nanostructures and large open channels at the nano and micro scale offer high surface area and facilitate better transport of ions and electrolytes. Besides, the swollen state of CPF hydrogel film may allow facile permeation of ions and electrons in between PANI chains which provides an additional effective surface area between molecular chains and the solution phase leading to high electrochemical performance. It is schematically represented in Fig. 4a.

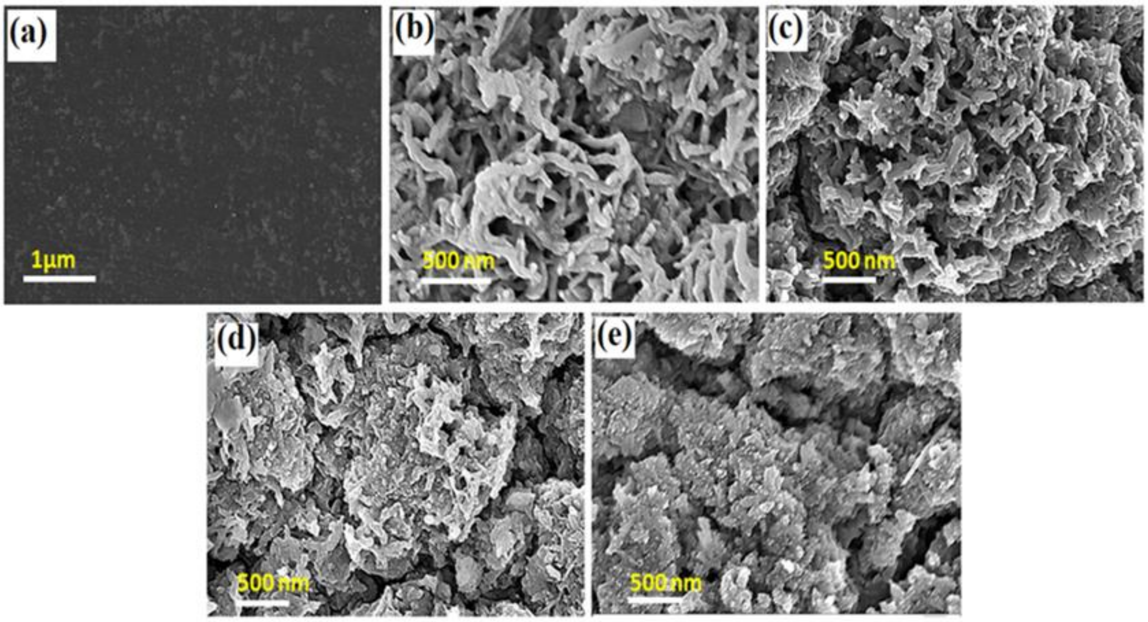

Fig. 3 SEM images of (a) chitosan, (b) CPF1, (c) CPF2, (d) CPF3 and (e) CPF4 films.

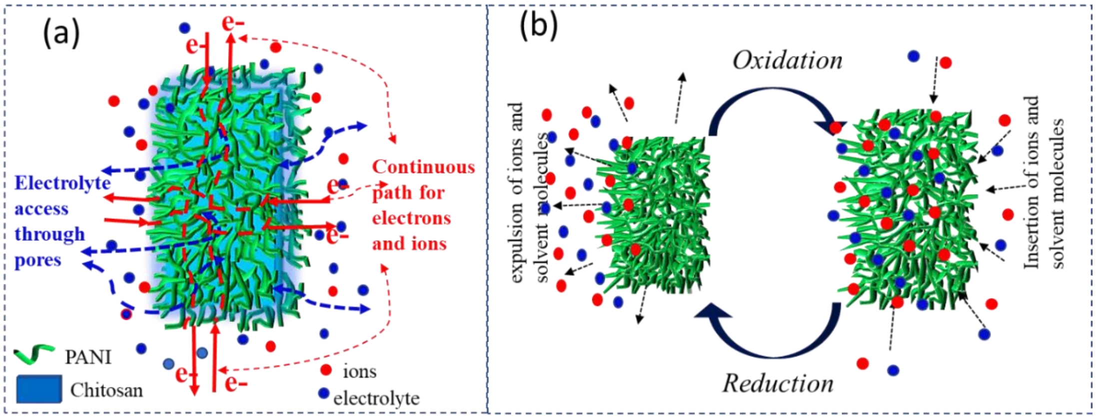

Fig. 4 (a) Schematic representation of structural features of CPF film enabling high electrochemical activity and (**b**) schematic representation of redox process of CPF films.

The EDX spectra (Fig. S2) of all the CPF films show a characteristic peak of Cl in addition to C, N and O, which is absent in chitosan film. It is introduced as the counter ion (Cl^-) during the acid doping of PANI confirming that polyaniline formed in the emeraldine salt form.

3.1 Electrochemical characterizations

The electrochemical activity of the hybrid film was analyzed by voltammetry. Fig. 5a is the cyclic voltammograms (CVs) of hybrid films recorded between the potential limit of -0.15 V to -0.8 V at a scan rate of 25 mV/s from 1 M HCl solution at room temperature in a three-electrode cell assembly using CPF films (area of 20 mm^2) as working electrodes, an Ag/AgCl (3 M KCl) as the reference electrode and platinum wire as the counter electrode, after stabilizing the CV through 20 consecutive cycles. All the CPF electrode shows two oxidation and two reduction peaks (Table S2) corresponding to leucoemeraldine ↔ emeraldine salt ↔ pernigraniline transitions.[61] The similarity of oxidation and reduction peaks with those of pure PANI approved that the electrochemical activity of CPF films was imparted by the electroactive component PANI. The hybrid film shows different current responses, which are mainly ascribed to the different polyaniline content and conductivity of the electrodes. The current response in CV increases as the number of times of coating increases and the highest currents were attained for CPF4 which is mainly ascribed to its highest PANI level, more porous structure and excellent conductivity.

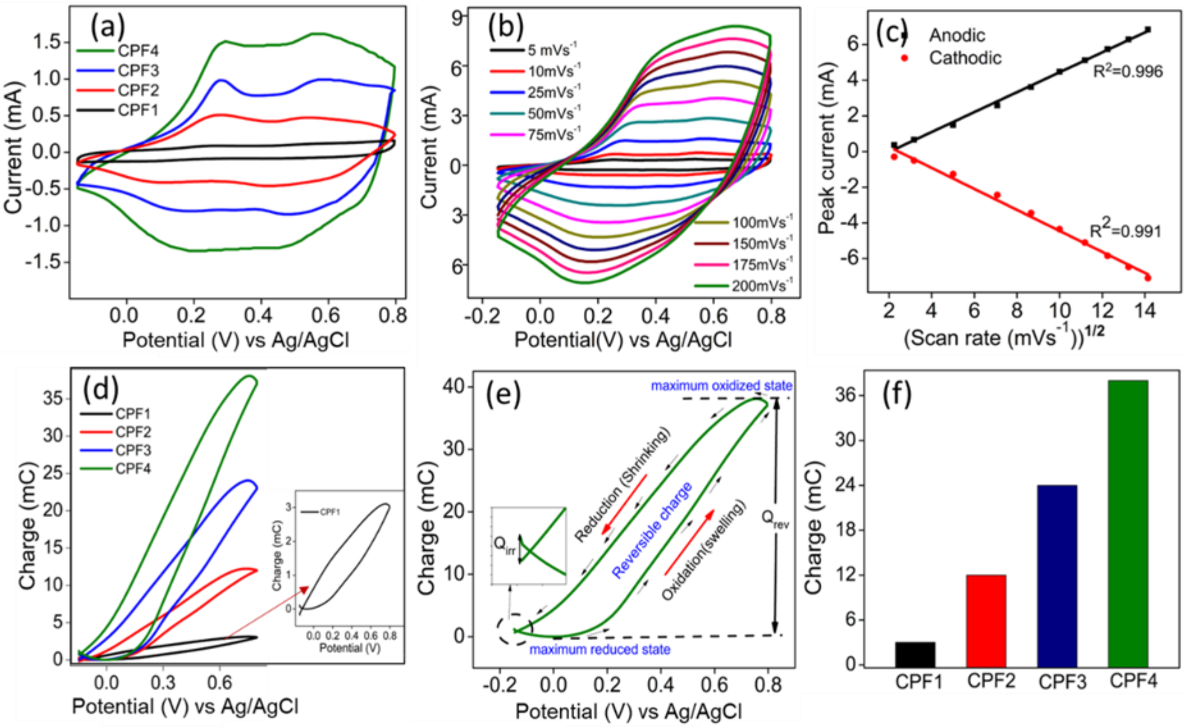

Fig. 5 (a) CV plot of CPF films obtained at a scan rate of 25 mV s^{-1} from 1 M HCl, (b) CVs of CPF4 at different scan rates, (c) linear relation between the square root of scan rate and anodic and cathodic peak current of CPF4, (d) QVs of CPF films obtained by integration of CVs (Fig. 5a) (e) QV of CPF4 in detail and (f) redox charges of CPF films obtained from QVs (Fig. 5d).

The relationship between scan rate and oxidation/reduction peak current was analyzed to understand the nature of the electrode process. The CV responses of hybrid films recorded at various scan rates from 5 mV s^{-1} to 200 mV s^{-1} are represented in Fig. 5b (CPF4) and Fig. S3 (CPF1, CPF2, and CPF3). The anodic and cathodic peak currents of CPF4 film increase linearly as a function of the square root of the scan rate as depicted in Fig. 5c (that of other samples is given in Fig. S3), which indicates that the oxidation/reduction process in the CPF films electrode is controlled by ion diffusion.

Figure 5d represents the coulovoltammograms (consumed charge vs. applied potential) (QV) of CPF hybrid films obtained by the integration of the current from respective CVs obtained at the scan rate of 25 mV s^{-1} from 1M HCl solution depicted in Fig. 5a. The QV gives the information regarding the involved charge (both reversible and irreversible charge) during cyclic oxidation-reduction at a particular potential range of the electroactive materials.[62] The QV of CPF4 is separately shown in Fig. 5e and shows that it constitutes a distinct closed loop on the right side which describes the presence of reversible oxidation (positive increment of charge) and reduction (negative increment of charge) reaction of CPF film and has a very small open fraction on the left bottom side (inset of Fig. 5e) which related to the irreversible reduction processes takes place in parallel to film reduction such as the hydrogen evolution. The minima of QVs are considered as the zero-charge reference and the closed-loops of QV account for the redox charge of the corresponding CPF film. The extension of the reversible oxidation/reduction reaction of each film is defined by the consumed reversible charge (Q_{redox}) which is obtained from the difference between the closed QV loop maximum and minimum.[63] The charge consumed by the reversible redox processes of the hybrid films is 3, 12, 24, and 38 mC respectively for CPF1, CPF2, CPF3 and CPF4 (Fig. 5f). The extension of the reversible redox reaction increases with increasing PANI content in the film. That is, higher PANI content (higher active center) promotes a larger number of ions exchanged during the reaction and thus concomitant consumption of higher oxidation/reduction charge.

3.2 Electrochemical sensing characteristics of hybrid films

The electrochemical reaction taking place in the CPF hybrid film that drives reversible variations can be written as follows Eqs. (5) and (6):

$$(\mathrm{PANI}^*)_{\mathrm{Solid}} + \mathrm{n}(\mathrm{X}^-)_{\mathrm{Solution}} + \mathrm{m}\ (\mathrm{H_2O}) \rightleftharpoons [(\mathrm{PANI})^{\mathrm{n}+}(\mathrm{X}^-)_{\mathrm{n}}(\mathrm{S})_{\mathrm{m}}]_{\mathrm{gel}} + \mathrm{ne}^- \qquad (5)$$

and

$$[\mathrm{H_oPANI}^*] \rightleftharpoons (\mathrm{PANI}) + \mathrm{oH}^+ + \mathrm{oe}^- \qquad (6)$$

The overall reaction can be written as Eq. (7):

$$(\mathrm{H_oPANI}^*)_{\mathrm{solid}} + \mathrm{n}(\mathrm{X}^-)_{\mathrm{el}} + \mathrm{m}\ (\mathrm{S}) \rightleftharpoons [(\mathrm{PANI})^{\mathrm{n}+}(\mathrm{X}^-)_{\mathrm{n}}(\mathrm{S})_{\mathrm{m}}]_{\mathrm{gel}} + \mathrm{oH}^+ + (\mathrm{n}+\mathrm{o})\mathrm{e}^- \qquad (7)$$

Where $PANI^*$ or H_oPANI^* indicates the active center (polyaniline) in the PANI/Cs hybrid film. Here, the forward process indicates the anodic oxidation, while the reverse process represents the cathodic reduction. During the oxidation process, the positive charges are generated on PANI polymer chains by the extraction of electrons. Hence, the anion (X^-) from the electrolyte along with solvent molecules (S) are inserted into the polymer chain for charge and osmotic balance, followed by the expulsion of the proton, which promotes polymeric swelling. All these processes are reversed during reduction, protons are reduced and incorporated into the polymer chain along with X^- and solvent molecules are expelled out, which promotes polymeric shrinking. The schematic representation of the electrochemical process is presented in Fig. 4b.

That is, during the electrochemical reaction (considering oxidation), the composition of polymer changes [$PANI^*$] and forms a dense polymer gel $[(PANI)^{n+}(X^-)_n(S)_m]$, not through a single step, but through *n* consecutive steps of one electron extraction per step, hence generation of one polaron on the chain per step. Because, the energy required for extraction of the first, second, third...nth electron from the chain is different. Thus, the continuous variation of composition under faradaic control by continuous extraction or insertion of electrons from the polymer chains becomes responsible for the changes in the composition-dependent material properties. In another way, the reversible reaction drives the cooperative actuation (swelling- shrinking) of the polymeric chains of hybrid film, and the number of exchanged ions and solvent molecules and the volume variation, *etc*. must have dependent on the number of electrons involved (charge) in this electrochemical reaction (Faraday’s law).[64]

The electrochemical reactions of conducting polymers (Eq. (7)), work outsides the equilibrium condition (there is a continuous composition variation during the reaction). So, Otero et al. reformulated the Le-Chatelier principle that can be applied to such systems: any chemical or physical perturbation of the constant reaction rate (during the flow of a constant current) will shift the reaction overpotential (energy of the electrons in the system) to fit the new imposed energetic (charge × potential) condition (Otero’s principle). It means that, at constant current flow, the evolution of potential, hence consumed electrical energy, during the reaction of conducting polymer is expected to respond to or sense the physical and chemical conditions of the reactive material (CPs) Thus, for any electrochemical device based on the conducting polymer reaction (supercapacitors, batteries, actuators, smart windows, *etc*) the potential evolution and consumed electrical energy during working will respond to or senses the changes of internal and surrounding conditions.[65,66]

The sensing properties of the PANI, driven by the electrochemical reaction, by the potential evolution (E) under the flow of a constant current are described by the relation (for the anodic process) (Eq. (8)):

$$E_a = E_0 + \frac{RT}{(1-\alpha)nF}\left(\ln\left(\frac{i_a}{FV}\right) - x\ln[X^-] - y\ln[PANIH_0] - zpH - \ln k_{a0}\right) \quad (8)$$

The oxidation of a polymeric chain occurs through the extraction of the n electrons through n consecutive steps of one electron per step, the most general equation for the potential of the material as a function of the different variables is given by the relation (Eq. (9)):

$$E_n(t) = E_0 + i_a Z + (n-1)\Delta E + \frac{RT}{(1-\alpha)nF} \left[\ln\left(\frac{i_a}{FV}\right) - x\ln[Cl^-] - y\ln\left([PANIH_0] - \frac{i_a t}{FV}\right) - zpH - \ln k_{a0}\right] \quad (9)$$

In the above equations, Ea is the anodic potential, E_0 is the standard potential; R is the universal gas constant; T is the reaction temperature; i_a is the applied anodic current; n is the number of consecutive electrons extracted from a chain; α is the symmetry factor; F is the Faraday constant; V film volume; X^- is the concentration of anions/counterion in solution; t is the time of flow of the constant current; ka_0 is the rate constant or rate coefficient for $E = E_0$; x, y, and z are the reaction orders for the concentration of the anions $[X^-]$ in solution, the active centers in the film [PANI] initially present at the beginning of the oxidation, and proton transferred with polymer chain respectively; Z is the electrochemical impedance of the system and ΔE is the potential increment for the extraction of (n-1)th and nth electrons from the same polymeric chain. Eq. (9) describes the potential evolution during the reaction for the system working outside the equilibrium, which is the function of the concentration of active center, applied current, electrolyte concentration and temperature. Besides, the electrical energy (U) consumed by the film during oxidation/reduction can be obtained in terms of potential evolution (E) and the flowing current (i) as Eq. (10),

$$U = i\int E\,dt \quad (10)$$

where ‘i’ is the constant driving current and ‘E’ is the potential change along the time ‘t’ of the current flow. By substituting Eq. (9) for E, a quantitative relation for consumed energy in terms of experimental variables can be obtained as similar to Eq. (9) and both these equations reveal that the potential evolution (E) and consumed electrical energy (U) during the redox reactions of conducting polymers will sense the reaction working in chemical and physical conditions. Similarly, the sensing equations, in terms of potential evolution and consumed electrical energy, for the cathodic process can also be deduced.

The above description of the electrochemical reaction of polyaniline clearly states that any device working based on the electrochemistry of polyaniline will be capable of sensing working and ambient variables (such as chemical concentration, current, and temperature) through the potential evolution and/or consumed electrical energy. It describes the possibility of several tools working simultaneously in one device.

The sensing characteristics of CPF hybrid films towards working/ambient conditions were monitored by recording chronopotentiograms under galvanostatic conditions. That is the film was subjected to consecutive square waves of current and the resulting chronopotentiograms were used for the analysis in all the cases (Fig. S4). The chronopotentiometric responses are almost identical from the second cycle onwards which indicates that the electrochemical activity of the film is highly reproducible (Fig. S4). Hence, the third cycle was used for the analysis in all the cases. The sensing of flowing current, temperature and concentration of the electrolyte were studied from the chronopotentiograms obtained from the constant charge experiments and consumed electrical energy as a sensing parameter.

3.2.1 Sensing of electrical working condition

For studying the sensing of electrical conditions (*i.e.*, flowing current) by the CPF hybrid films, chronopotentiograms were recorded from the aqueous solution of 1M HCl corresponding to three consecutive square waves of currents of different magnitudes ranging from ± 0.1 mA to ± 1 mA, by adapting the time of the square waves to attain a constant oxidation and reduction charges ($Q = i \times t$, kept constant) for obtaining the same initial and final oxidation states or same reaction extension in each experiment. It is equivalent to galvanostatic charging and discharging at different currents corresponding to the constant charged state. Here, the chronopotentiograms of each hybrid film were recorded at a constant charge which is equal to their redox charge obtained from the coulovoltammograms at the scan rate of 25 mV s^{-1} (Fig. 5d). The normalized chronopotentiometric responses for the anodic and cathodic processes of each hybrid films are shown separately in Figs. 6a-d and Figs. 6e-h, respectively. As the applied current increases, the potential evolution occurs to higher positive potential values for the anodic process and higher negative potential values for the cathodic process.

The consumed electrical energy (U), during each oxidation or reduction process was calculated using Eq. (10). Fig. 7a shows that the consumed electrical energy during the redox reaction has a linear dependence on the applied electric current for all the films. Thus, it indicates that the reaction energy senses or responds to locally imposed electrical conditions. The slope of each current versus electrical energy calibration curve (Fig. 7a) indicates the sensitivity of the material as a sensor. The current sensitivity corresponding to the anodic and cathodic processes of each film is represented in Fig. 7b. The highest sensitivity is obtained for CPF4, 14.14 mJ mA^{-1} and -14.35 mJ mA^{-1} for the anodic and cathodic processes,

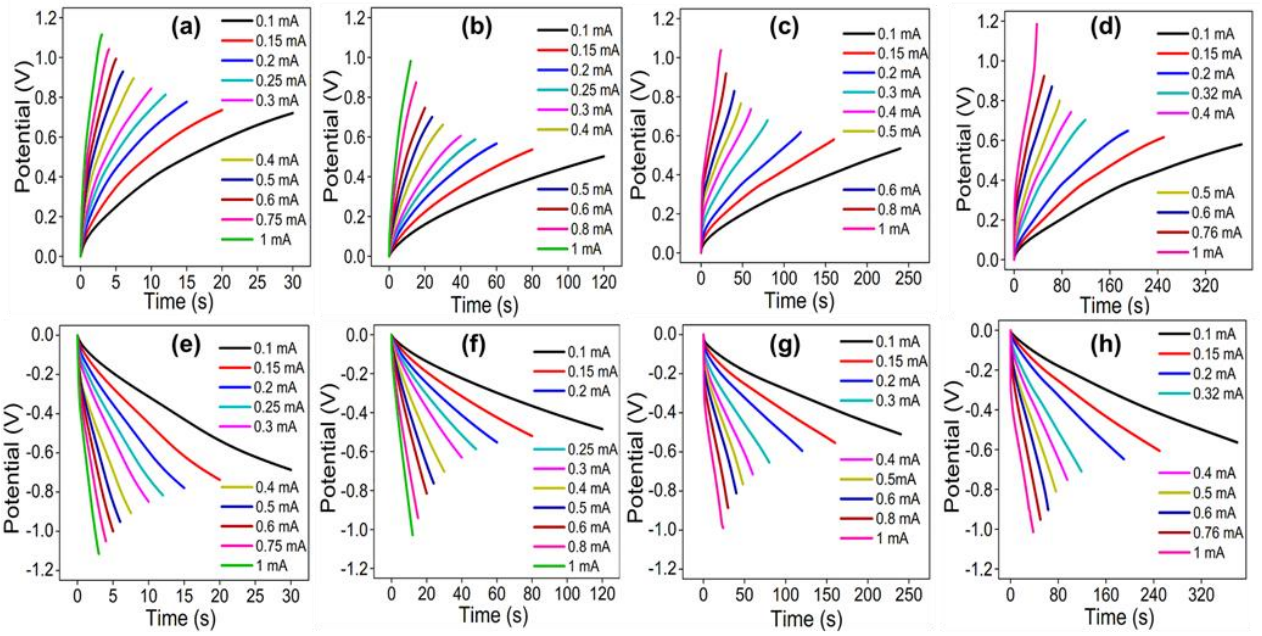

Fig. 6 (a-d) Anodic and (e-h) cathodic chronopotentiograms obtained when different currents were applied to CPF1 (a & e), CPF2 (b & f), CPF3 (c & g) and CPF4 (d & h), respectively, by passing a constant electrical charge in 1 M HCl solution.

respectively. The sensitivity gradually increases from CPF1 to CPF4, as the number of times of coating of polyaniline increases, due to the higher number of polymer active sites.

3.2.2 Sensing the thermal condition

Eq. 9 reveals that the potential evolution, hence the consumed electrical energy (according to Eq. (6)), during the reaction is a function of the working temperature. To study the temperature sensing characteristics, the hybrid film was subjected to consecutive square current waves of ± 0.2 mA at a different temperature in 1M HCl solution for a constant period of time to keep the charge constant (i × t = constant). The temperature sensing characteristics of all four synthesized films were carried out at their respective redox charges obtained from coulovoltammograms (Fig. 5d). The obtained stationary and normalized chronopotentiograms corresponding to oxidation and reduction processes of hybrid films are depicted in Fig. 8. As described by the Arrhenius temperature dependence of the rate of reaction, the rate of an electrochemical reaction is expected to increase with increasing experimental temperature. The hybrid films are working under constant current flow (constant reaction rate). As the temperature increases, the available thermal energy increases and there occur faster and longer conformational movements of the polymer chains. Thus, the electrode reaction requires lower electrical energies compared to that required at the lower temperature for attaining the same reaction extension. It means that the material potential should evolve at lower values during reactions taking place at higher temperatures to go from the same initial state to the same final state every time.

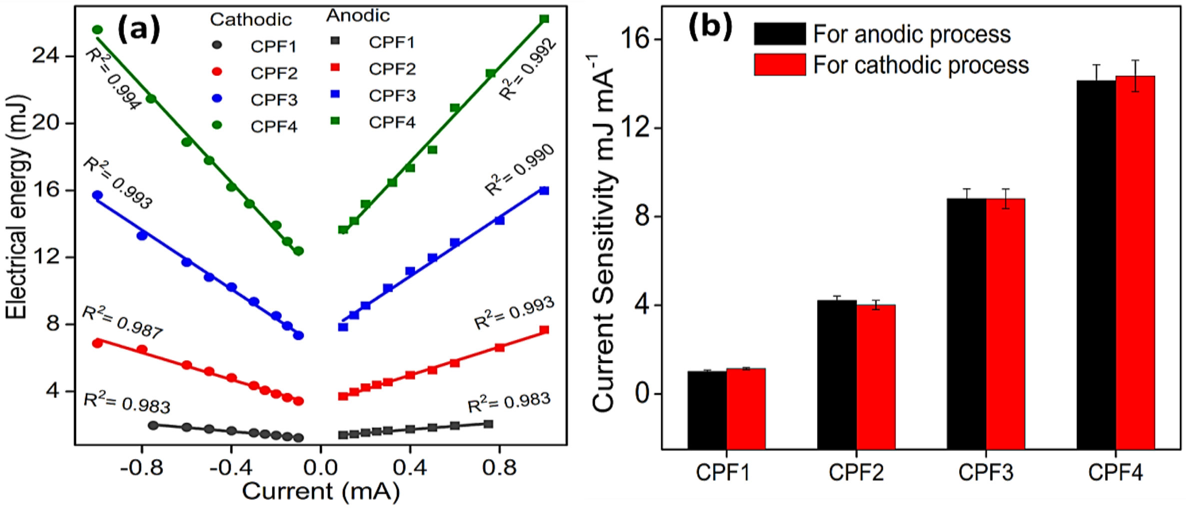

Fig. 7 (a) The linear variation of consumed electrical energy with the working current of CPF films, and (**b**) effect of coating of PANI film on current sensitivity.

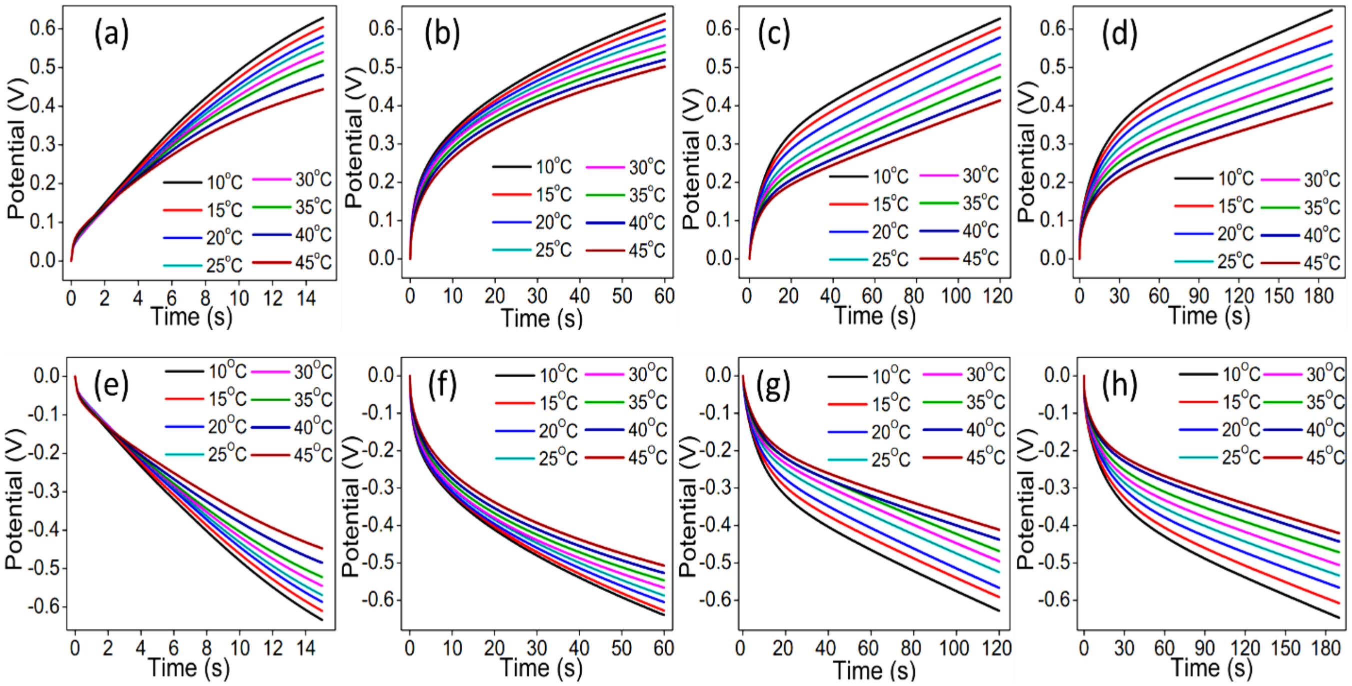

Fig. 8 (a-d) Anodic and (e-h) cathodic chronopotentiograms obtained at different working temperatures for CPF1 (a & e), CPF2 (b & f), CPF3 (c & g) and CPF4 (d & h), respectively, by passing a constant electrical charge in 1 M HCl solution.

The electrical energy required during each oxidation-reduction reaction at different temperatures is obtained by the integration of corresponding chronopotentiograms according to Eq. (6). The consumed electrical energy during the anodic and cathodic process of CPF film has a linear dependence on the working temperature as depicted in Figs. 9a and 9b. It reveals that CPF films can act as a sensor of the working temperature. The slope of calibration curves represents the sensitivity towards the working temperature and the highest sensitivity of -198.84 µJK^{-1} and -188.83 µJK^{-1} for anodic and cathodic processes, respectively, obtained for CPF4 film. The sensitivity gradually increases from CPF1 to CPF4 (Fig. 9c), because, the active mass (PANI content) increases as the number of times of coating increases, then the resulting film has a greater number of polymer active sites.

3.2.3 Sensing the chemical condition

Equation (9) also reveals that the potential evolution, hence the consumed electrical energy (according to Eq. (10)) during the reaction also has a logarithmic dependence on the

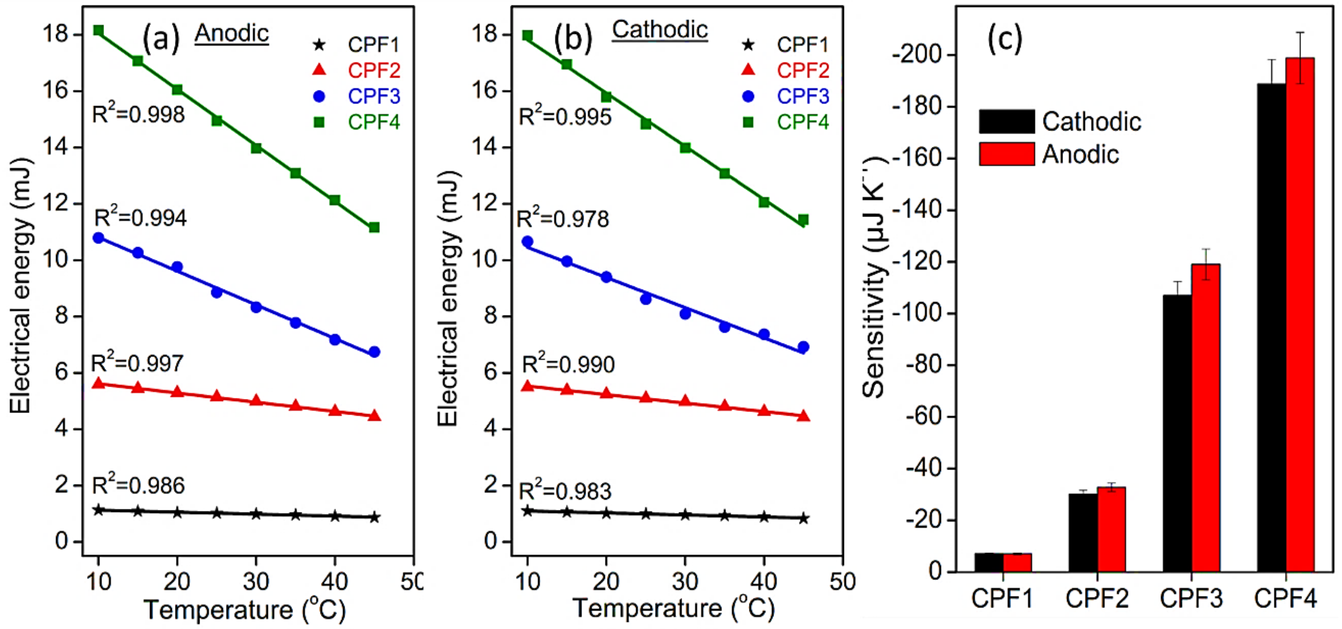

Fig. 9 The linear variation of consumed electrical energy for (a) anodic and (b) cathodic process with the working temperature of CPF films and (c) effect of coating of PANI on temperature sensitivity.

concentration of the electrolyte (counter anion). To investigate the electrolyte concentration sensing characteristic of the CPF films, the chronopotentiograms were recorded from various concentrations of HCl ranging from 1 M to 0.05 M at a constant square wave of current (±0.2 mA) for a particular period of time to keep a charge (I × t) constant (same reaction extension) in each experiment at room temperature. It is equivalent to galvanostatic charging and discharging of CPF films at different concentrations of electrolyte corresponding to the constant charged state (Q=i × t=constant).

Figure 10 is the normalized chronopotentiometric responses for anodic and cathodic processes of CPF film at different concentrations of electrolyte. Figs. 10a-d correspond to the anodic and Figs. 10e-h correspond to the cathodic chronopotentiograms of the four hybrid films. The graphs show that, in each experiment, a sudden potential step at the initial stage of potential evolution, is due to various types of resistance offered by the film and electrolyte. After this initial stage, the potential gradually increases with time during the current flow by the PANI reaction. It is clear that, during the reversible oxidation/reduction of the polymer films, the anodic and cathodic potentials evolve at lower values during rising electrolyte concentrations, under constant charge. In other words, during the oxidation/reduction process, lower available energy (chemical potential) requires the consumption of higher electrochemical energy to attain the same charged state.

Upon integration of the chronopotentiometric responses at different concentrations, the electrical energy consumed during the reaction is obtained. Figs. 11a and b indicate the electrical energy consumed during the oxidation and reduction of CPF film, respectively, under constant charge, have a semi-logarithmic dependence (as in the sensing equation) with the electrolyte concentration, hence, capable to sense the chemical working condition. The slope of the calibration curve is the sensitivity of the hybrid films towards the concentration of electrolyte, and the highest sensitivity of -0.84 and -0.74 mJ M for anodic and cathodic processes, respectively, obtained for CPF4 film. As in the case of current sensing and temperature sensing the sensitivity gradually increases from CPF1 to CPF4 (Fig. 11c).

3.3 Supercapacitive studies

The charge storage performance of hybrid films was examined through CV and GCD analysis. The CVs (Fig. 5a) are non-rectangular curves with two pairs of redox peaks attributed to the faradaic pseudocapacitive dominance. Among all hybrid film, CPF4 have the largest enclosed area ascribed to the highest specific capacitance which is consistent with the conductivity of the films. The specific capacitance of the hybrid film electrodes was also calculated from the CV curves according to Eq. (1). The specific capacitance obtained for CPF1, CPF2, CPF3 and CPF4 are 48, 195, 309 and 468 mF cm^{-2}, respectively, at a scan rate of 5 mV s^{-1} (CVs at the scan rate of 5 mV s^{-1} are represented in Fig. S5).

Figure 12a represents the GCD curves of CPF hybrid films obtained at a current density of 0.4 mA cm^{-2} within the potential range of -0.15 to 0.8 V. The discharge time is the indication of the energy storage property of the electrode material. Their deviation from linearity is caused by the redox process, demonstrating their pseudocapacitive behavior. CPF4 shows the longest discharge time among these four hybrid films corresponding to its best electrochemical capacitive property, consistent with its highest electric conductivity which is beneficial to promoting the electron transfer process. The areal specific capacitance values are calculated using Eq. (2), the values for CPF1, CPF2, CPF3 and CPF4 are 31, 59,

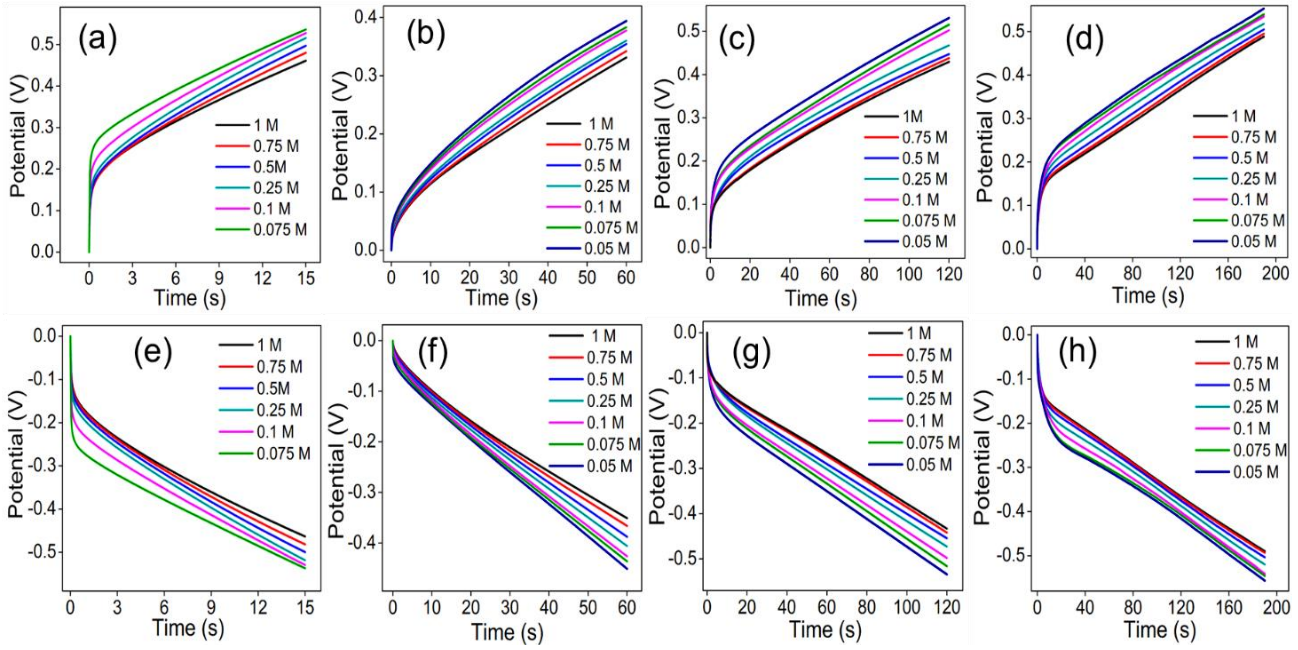

Fig. 10 (a-d) Anodic and (e-h) cathodic chronopotentiograms at different electrolyte concentrations obtained for CPF1 (a & e), CPF2 (b & f), CPF3 (c & g) and CPF4 (d & h), respectively, by passing a constant electrical charge.

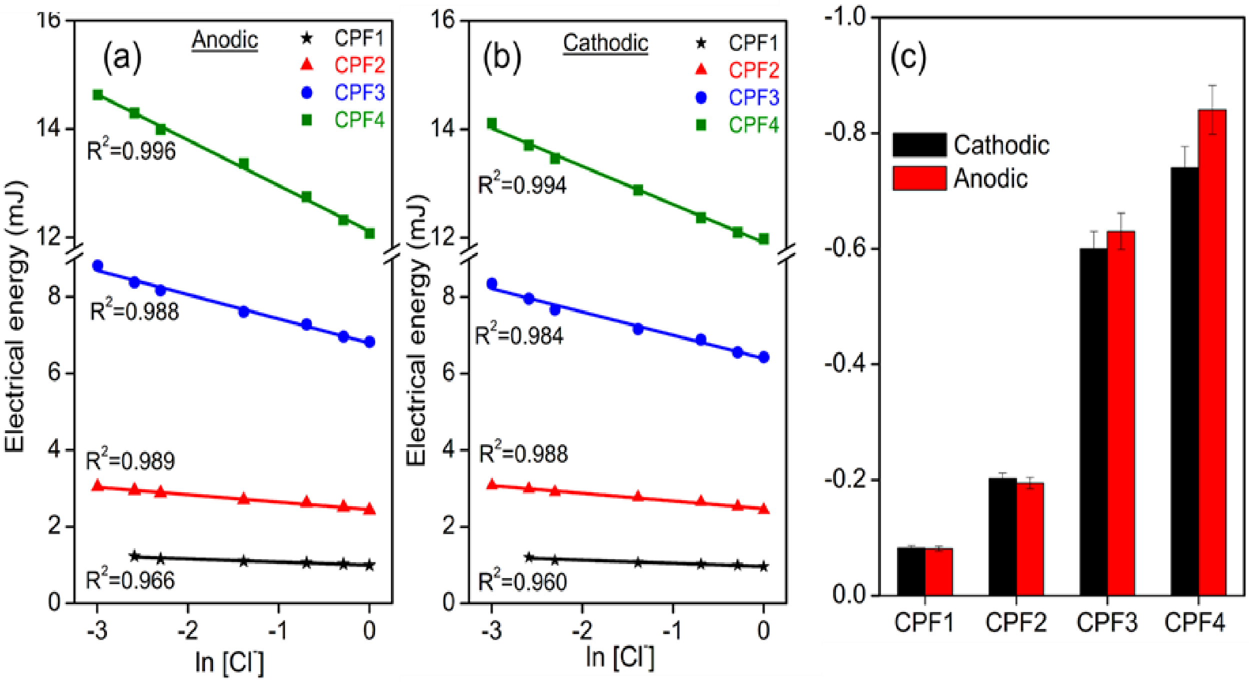

Fig. 11 Linear variation of consumed electrical energy for (a) oxidation and (b) reduction process with the electrolyte concentration of CPF film and (c) effect of coating of PANI on concentration sensitivity.

146 and 241 mF cm^{-2} respectively. Fig. 12b shows the GCD curves of CPF4 at different current densities. The GCD curves are almost symmetrically shaped, indicating that the hybrid films have superior electrochemical reversibility and excellent coulombic efficiency. The variation of specific capacitance as a function of current density from 0.4 to 4 mA cm^{-2} corresponding to CPF4 is represented in Fig. 12c. As usual, the capacitance decreases as the current density increases due to the provision of less time for the electrolyte ions to diffuse into active sites and interact with active material at the high current density. Interestingly, it is noted that the 79 % capacitance retained after a ten times increase of current density in the case of CPF4 which indicates that the material has good kinetics and rate capability due to the presence of chitosan which facilitates ion transport and it is much better than reported conductive-polymer-based electrodes which typically gives 50–60% capacitance retention at a 10-fold higher current density.[67,68] The relationship between specific capacitance and scan rates for CPF4 is plotted in Fig. 12d. The specific capacitance decreases with scan rate because the electrolyte ions do not sufficiently reach the internal part of the electrode material effectively at higher scan rates.

EIS was performed to analyze the fundamental electrochemical behaviour of CPF films. Fig. 12e represents the Nyquist plot of all four CPF films (The inset shows the magnified plot of CPF1 and CPF2) which have a small semicircle part at the high frequency region and a nearly straight oblique line in the low-frequency region. The semicircle mainly depicts the charge transfer process at the electrode-electrolyte interface and whose intercept to the real axis at the high frequency region meant for the equivalent series resistance (ESR), including solution resistance, the internal resistance of materials and the contact resistance between the electrode and electrolyte. All the CPF films have very low ESR values which is attributed to the high hydrophilicity of CPF films as well as a good interconnection between the electrode and the electrolyte, thereby efficient access of electrolyte ions to the PANI through the swollen chitosan matrix. The semicircle diameter reflects the migration impedance of charges or charge transfer resistance (R_{ct}). The Nyquist plot showed a very small semi-circle in the high frequency region which is ascribed to the smooth charge transfer between the electrode and the electrolyte because the chitosan in the hydrogel film act as a continuous channel for electrons and ions. The diameter of semicircles decreases from CPF1 to CPF4 pointing out declining the charge transfer resistance and increasing electron transfer in the same order due to increasing the conductivity. The oblique line refers to the diffusion-limited ion transport process across the electrode surfaces, its slope gives the diffusion impedance and a larger slope of the line indicates the higher diffusion rate of ions. Here, the CPF films show a relatively large slope because of the highly porous nature of CPF films as evidenced by SEM images, which facilitate ion diffusion. CPF4 exhibits the highest slope compared to other hybrid films, indicating its higher ion diffusion efficiency. The results of the EIS analysis are consistent with CV and GCD results.

The long-term cycling stabilities of CPF4 hybrid film electrodes were monitored by GCD over 1500 cycles at 2 mA cm^{-2} as depicted in Fig. 12f. CPs usually suffer poor cyclic stability due to the structural degradation of the polymer chain caused by the intercalation/deintercalation (swelling/shrinking) of ions during the repeated charge/discharge process. One of the recent studies shows that the polyaniline doped with HCl

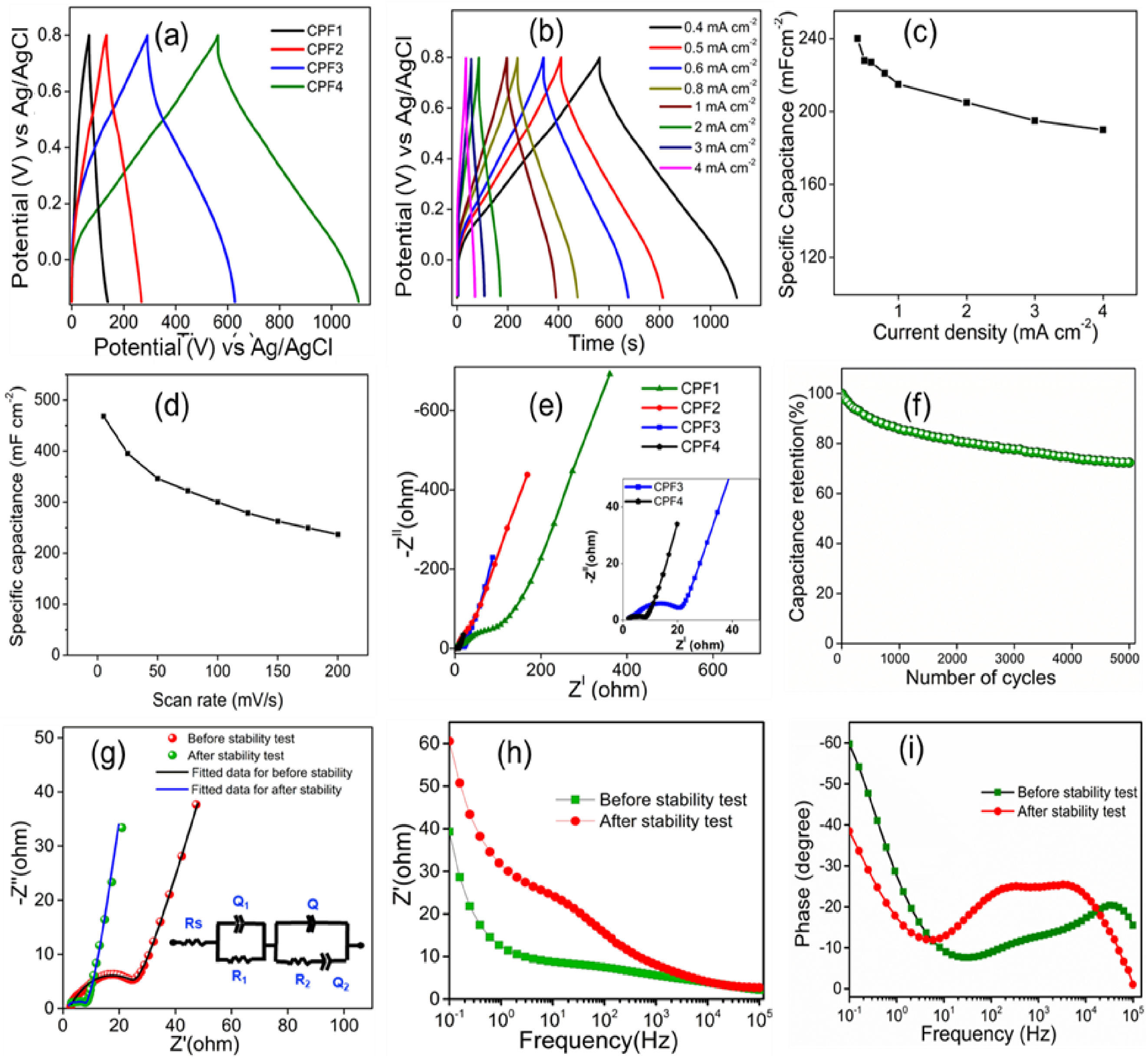

Fig. 12 (a) GCD curves of CPF electrodes at a current density of 0.4 mA cm^{-2}, (b) GCD curves of CPF4 at different current densities, (c) variation of specific capacitance of CPF4 electrode with current density, (d) variation of specific capacitance of CPF4 with scan rate (e) Nyquist plot of CPF electrodes (f) cycling stability of CPF4 for 5000 cycles, (f) Nyquist plot of CPF4 before and after stability test (inset shows the fitting circuit) and (g) and (h) are Bode plots before and after stability test.

and H_2SO_4 has capacity retention of only around 50% of their initial value after 1500 cycles of charge discharge.[69] But, this CPF4 hybrid electrode shows good electrochemical stability, which retains 72 % of its initial capacitance after 5000 cycles, attributed to the strong synergy existing between chitosan and polyaniline resulting in a supportive and protective effect on PANI during swelling and shrinking. EIS analysis was performed before and after the cycling stability test to further investigate the capacitive, resistive, and charge-transport properties of the CPF4 electrode during long-term cycling. Fig. 12g represents the Nyquist plot before and after the stability test. The solution resistance, *i.e.*, the X-axis intercept at high frequency, as well as charge transfer resistance, *i.e.*, the diameter of a small semicircle in a high-frequency region, increased after long-term cycling. This might be due to the depletion of active sites during a prolonged cycling test. Fig. 12h is the Bode plot showing the relationship between frequency and impedance also indicates that the resistance CPF was increased after prolonged cycling supporting the above observation. Fig. 12h represents the Bode plot showing the relationship between frequency and phase angle. The maximum phase angle obtained at low frequency (0.01 Hz) was 59.75° and 38.48°, respectively, before and after the cycling test. In general, the maximum phase angle of 90° at low-frequency approaches reveals a pure capacitive nature of the electrode. the phase angle value revealed that the CPF electrode has a sufficient capacitive contribution. The shift in phase angle from this ideal value (90°) indicates the pseudocapacitive nature of the CPF electrode.

In addition, the charge storage behaviour of CPF4 hybrid film can be explored by applying the power law which relates the current '*i*' at a particular potential with the scan rate '*v*' by the following Eqs. (11) and (12):

$$i = av^{b} \tag{11}$$

$$\log(i) = \log(a) + b\log(v) \tag{12}$$

Both a and b are constants. The value of b at different potentials can be obtained by plotting *log*(*i*) against *log*(*v*) as shown in Fig. 13a. In general, b = 0.5 corresponds to the ideal diffusion controlled Faradaic process, while b = 1 corresponds to the outer surface non-diffusion-controlled process (double layer phenomenon).[70] The b values at the different potentials for the anodic process are depicted in Fig. 13b. The b values lie between 0.5 and 1, which means that the charge storage comes from the both diffusion controlled and the capacitive (double layer) process. Then, the capacitive and diffusive contribution in CPF4 film is quantified by Dunn's method.[70] The total current contribution at a potential is the sum of diffusive-controlled and capacitive currents which is defined as;

$$i(V) = i_{capacitive} + i_{diffusion} = k_1 v + k_2 v^{1/2} \tag{13}$$

divide Eq. (13) by $v^{1/2}$ on both sides,

$$i(V)/_{v^{1/2}} = k_1 v^{1/2} + k_2 \tag{14}$$

Here, one can determine the slope k_1 and the intercept k_2, while plotting of $i(V)/v^{1/2}$ vs $v^{1/2}$. to obtain capacitive and diffusive current at a particular potential of 'V'.

Figure 13(c) illustrates the graphical representation of the current contribution by the capacitive and diffusion-controlled process for sweep rates of 5 mV s^{-1}. The highlighted area with a navy blue color reveals the capacitive contribution in the CV curve. At the lower scan rate of 5 mV s^{-1} the contribution from the diffusion limited faradaic process is 51% and from the non-faradaic process is 49 %. The bar plots of percentage contribution from the capacitive and diffusive process for different scan rates are presented in Fig. 13(d). As increasing the scan rate, the diffusive contribution is decreased while the capacitive contribution is increased. At the highest scan rate of 100 mV s^{-1} the CPF4 electrode has a capacitive contribution of 82 % in comparison to a diffusive contribution of 18%. This is because, at lower scan rates, enough time is available to complete the redox reaction, thereby a larger diffusive contribution in the overall capacitance.

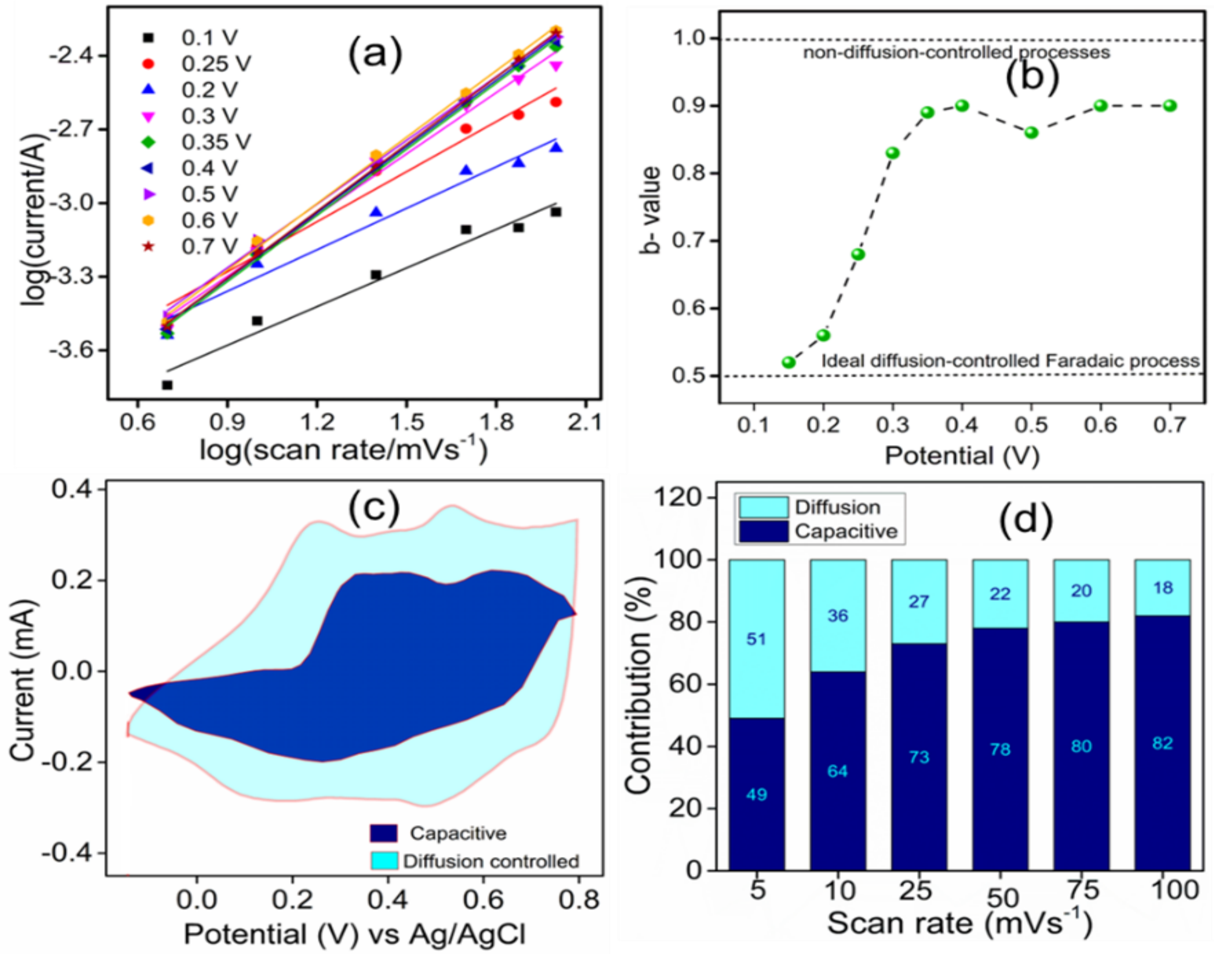

Fig. 13 (a) The determination of b values at different potential regimes, (b) the obtained b values, (c) separation of the capacitive and diffusion currents at a scan rate of 5 mV s^{-1} and (d) contribution ratios from non-faradaic double layer process (capacitive) and diffusion limited oxidation/reduction of CPF4 at various sweep rates.

3.4 All-solid-state CPF device

To demonstrate the feasibility of CPF hybrid film as a sensing supercapacitor, a symmetric solid-state supercapacitor device was fabricated by sandwiching two CPF4 films with filter paper and PVA–H_2SO_4 gel as the separator and electrolyte, respectively (detailed fabrication procedure given in experimental section). The performance of the device was tested by CV, GCD, and EIS methods in two electrode modes. The CV diagrams obtained at different scan rates are presented in Fig. 14a. Almost similar and symmetrical shapes of these CVs suggest the good capacitive behavior of the supercapacitor. From CV the areal specific capacitance obtained for the device is 222 mF cm^{-2} at a scan rate of 5 mV s^{-1}.

The GCD pattern obtained at different current densities is given in Fig. 14b. The specific capacitance of this supercapacitor was calculated based on the total area of this device. This supercapacitor demonstrates good areal specific capacitance of 111 mF cm^{-2} at a discharge rate of 0.4 mA cm^{-2}. It is higher than those of various polyaniline-hydrogel-based supercapacitors reported in the literature (Table S3). Fig. 14c and Fig. 14d reveal that the specific capacitance decreases with increasing specific current and scan rate, respectively because the electrolyte ions do not get enough time to interact with electrodes at higher current density and higher scan rate. The cyclic stability of the supercapacitor is one of the significant aspects of its practical application. Fig. 14e shows the graph of the cycling stability of the device analyzed at a scanning rate of 4 mA cm^{-2} for 5000 continuous cycles. The device retains 74 % of its initial specific capacitance after 5000 charge-discharge cycles suggesting the long-term electrochemical stability of the device.

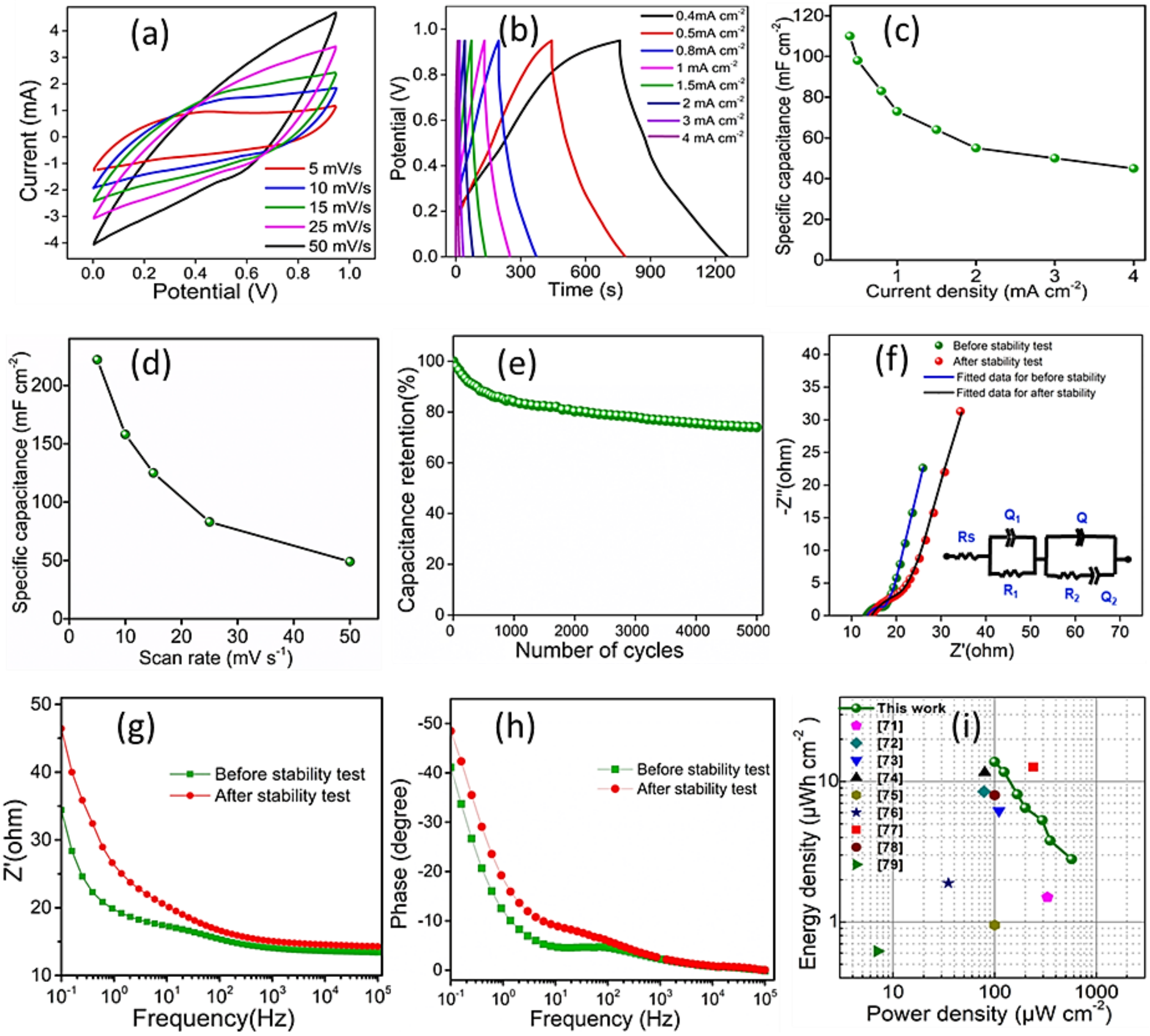

Fig. 14 (a) CV curves of CPF device at different scan rates, (b) GCD curves of CPF device at different current densities, (c) variation of specific capacitance of device with current density, (d) variation of specific capacitance of device with scan rate (e) cycling stability of the device, (f) Nyquist plot of the device before and after stability test (inset shows the fitting circuit) and (g) and (h) are Bode plot of the device before and after stability test (i) Ragone plot of the device in comparison to other PANI-hydrogel based devices in literature.

The EIS spectra were also recorded before and after the stability test for the device to further analyze and quantify the electrochemical kinetics parameters. The Nyquist plot given in Fig. 14f and the inset show an equivalent circuit used for fitting the experimental data obtained by Zman software and the parameters are summarized in Table S4. The figure shows a semicircle at high frequency resulting from the parallel combination of resistance and capacitance as well as an inclined line in the low-frequency region that accounts for the diffusion of ions into the porous electrode. Before long-term cycling, the device has Rs of 13.45 Ω and Rct of 0.5 Ω, suggesting low internal resistance and fast charge transfer process even in PVA/H_2SO_4 hydrogel electrolyte, indicating the favorable electrochemical kinetics of fabricated supercapacitor. The Rs and Rct values slightly increased to 14.4 Ω and 1.26 Ω, respectively, after prolonged cycling evidencing the decreased performance after 5000 cycles. It may due to the unavailability of electrolytes in the bulk of the electrode from gel electrolytes and the depletion of active sites during long-term cycling. Bode plots (frequency vs impedance) exhibited in Fig. 12g also indicate that the charge transfer resistance of the device was increased after prolonged cycling supporting the above observation. Fig. 12h depicts the Bode plot showing the variation of phase angle with frequency. The maximum phase angle obtained at low frequency (0.01 Hz) was 41.1° and 48.5°, respectively, before and after the cycling test. The shift in phase angle from this ideal value for a double-layer capacitor (90°) indicates the pseudocapacitive nature of the device. The slight increase in phase angle after a long-term cycle may due to the depletion of the pseudocapacitive nature of the device.

Figure 14i represents the Ragone plot which shows the variation of the areal energy density and power density of the device. The fabricated supercapacitor has an energy density of 13.8 μWh cm^{-2} at a power density of 100 μW cm^{-2}. It demonstrates that the device can provide remarkably high energy densities at relatively high-power densities compared to those previously reported for various PANI-hydrogel supercapacitors[71-78] which are depicted in the Ragone plot and Table S3.

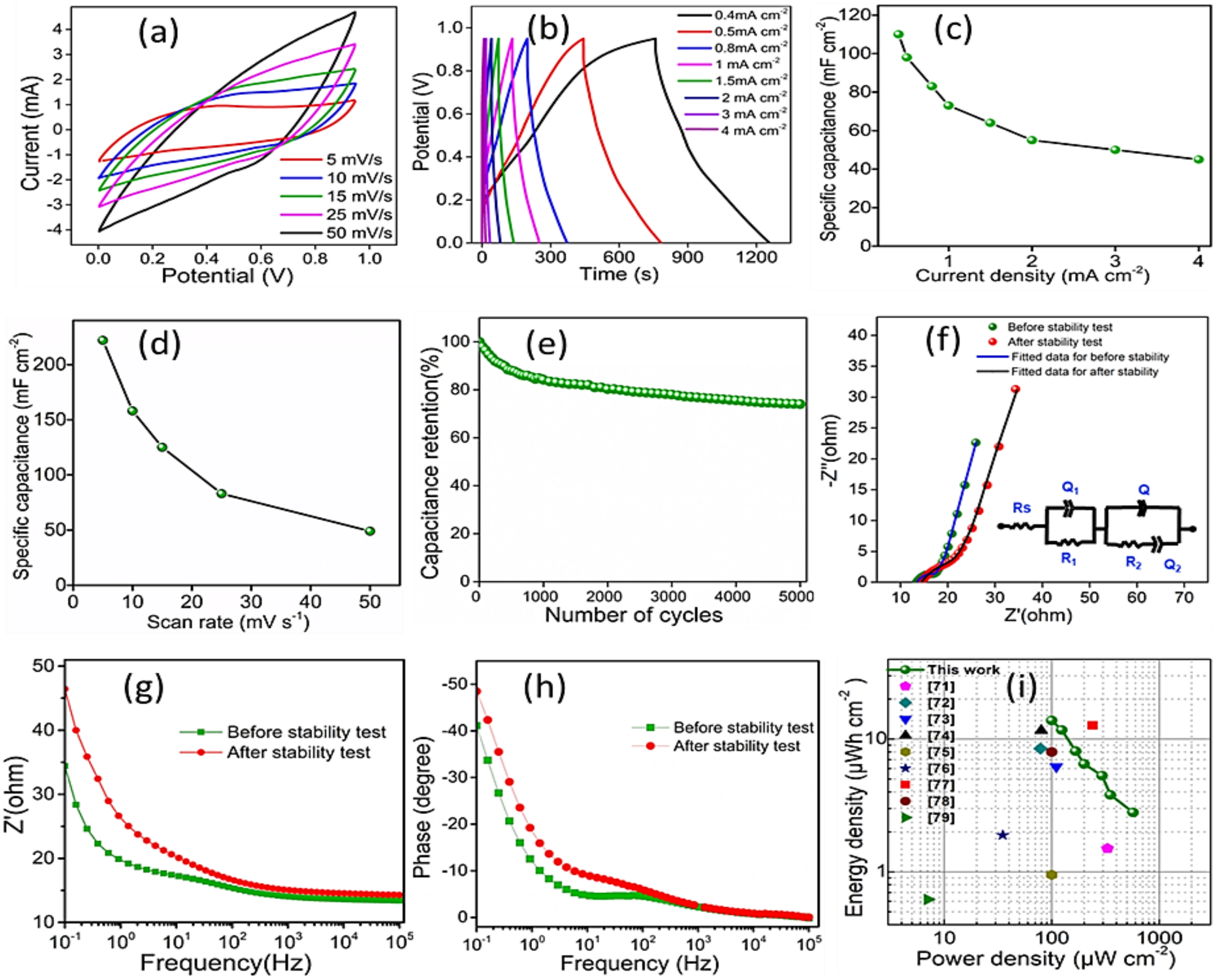

Fig. 14 (a) CV curves of CPF device at different scan rates, (b) GCD curves of CPF device at different current densities, (c) variation of specific capacitance of device with current density, (d) variation of specific capacitance of device with scan rate (e) cycling stability of the device, (f) Nyquist plot of the device before and after stability test (inset shows the fitting circuit) and (g) and (h) are Bode plot of the device before and after stability test (i) Ragone plot of the device in comparison to other PANI-hydrogel based devices in literature.

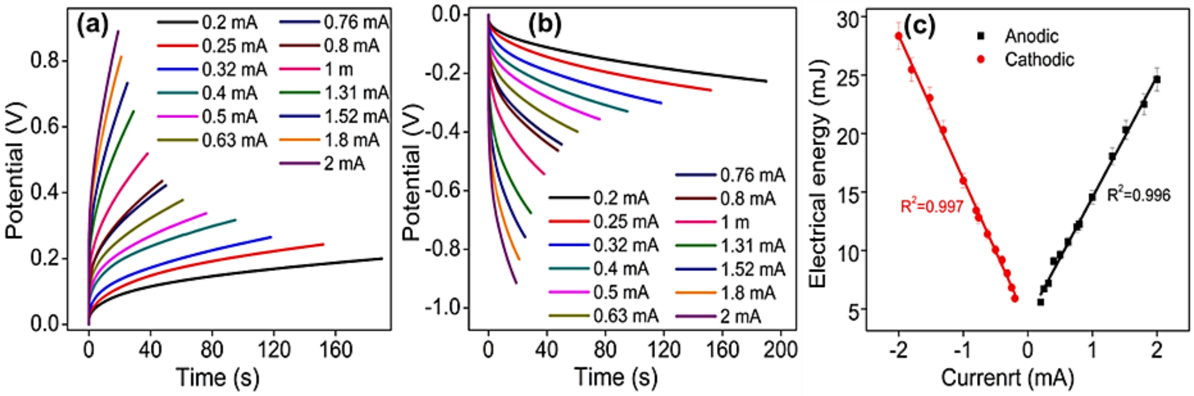

Fig. 15 Normalized (a) anodic and (b) cathodic chronopotentiograms of the device corresponding to different working currents at the constant charge of ±38 mC and (c) Linear variation of consumed electrical energy as a function of working current.

To demonstrate the sensing capability of the CPF supercapacitor towards the working condition, as a proof of concept, the current sensing characteristics of the device were analyzed in the two-electrode mode at a constant charge by chronopotentiometry (charging/discharging). Fig. S6 represents the steady state charging-discharging curve at different applied currents corresponding to the consumption of a constant charge of ±38 mC (keeping Q=i*t =constant, by adapting the time of charging and discharging to attain constant oxidation and reduction charges). The separate normalized chronopotentiometric responses for the anodic or oxidation (charging of 38 mC) and cathodic or reduction (discharging of 38 mC) processes of the device are shown in Figs. 15a and 15b, respectively. The electrical energy consumed during the anodic current flow (during charging) and cathodic current flow (during discharging) were obtained by integrating the area under corresponding chronopotentiometric curves and multiplied by the charging/discharging current according to Eq. (10). The consumed electrical energy has a linear dependence working current with excellent correlation along with well-defined sensitivity and reliability as depicted in Fig. 15c. It reveals that the CPF supercapacitor can able to sense its electrical working condition without the need of additional connectivity. The consumed electrical energy during the charging-discharging process can thus reveal information regarding the working ambient.

4. Conclusion

In this study, we introduce the concept of a self-sensing supercapacitor by adopting the PANI/ chitosan hybrid hydrogel free-standing film as an electrode whose faradaic electrochemical reaction (oxidation/reduction) is responsible for both the energy storage and sensing working conditions with the same connectivity. The conducting polymer-based supercapacitors (pseudocapacitors) undergo oxidation during charging and reduction during discharging. The variation of consumed electrical energy during these oxidation-reduction processes using CPF hybrid supercapacitor electrodes in the different working environments: electrical, thermal and chemical conditions were analyzed by the constant charge experiments and found that it has a linear dependence with applied current and temperature and has a logarithmic dependence with electrolyte concentration. The CPF hybrid electrodes have high electroactivity due to their porous structure which provides a high active surface area and easy access to the electrolyte as well as the hydrophilic chitosan act as a continuous channel for ions and electrons. As the proof-of-concept, a study from the perspective of material, we fabricated an all-solid-state supercapacitor device with CPF hybrid film and demonstrated its charge storage and sensing capabilities. The device shows a high specific capacitance of 111 mF cm^{-2} at 0.4 mA cm^{-2} and 222 mF cm^{-2} at a scan rate of 5 mV s^{-1}. A remarkable energy density of 13.8 μWh cm^{-2} at a power density of 100 μW cm^{-2} and reasonable cycling stability (74% capacitance retention after 5000 cycles) indicates strong synergy between chitosan and polyaniline. Along with charge storage capability, it has a well-defined sensitivity and reliability towards working conditions (current). The consumed electrical energy during the charging/ discharging process act as the sensing parameter. This integration strategy does not require additional connectivity for sensors and therefore, it gives a positive impetus for the development of a new generation of compact energy-related systems.

Acknowledgments

SMP and AS gratefully acknowledge the financial support received from UGC, India. LR acknowledges Kerala State Council for Science Technology and Environment (KSCSTE), Kerala, India for financial assistance. The authors acknowledge the CSIF - the University of Calicut for providing characterization facilities.

Conflict of Interest

There is no conflict of interest.

Supporting Information

Applicable.

References

[1] T. F. Otero, J. G. Martinez, Biomimetic intracellular matrix (ICM) materials, properties and functions, Full integration of actuators and sensors, *Journal of Material Chemistry B*, 2013, **1**, 26-38, doi: 10.1039/c2tb00176d.

[2] A. Eftekhari, L. Li, Y. Yang, Polyaniline supercapacitors, *Journal of Power Sources*, 2017, **347**, 86-107, doi: 10.1016/j.jpowsour.2017.02.054.

[3] E. W. H. Jager, E. Smela, O. Inganäs, Microfabricating conjugated polymer actuators, *Science*, 2000, **290**, 1540-1545, doi: 10.1126/science.290.5496.1540.

[4] F. García-Córdova, L. Valero, Y. A. Ismail, T. F. Otero, Biomimetic polypyrrole based all three-in-one triple layer sensing actuators exchanging cations, *Journal of Materials Chemistry*, 2011, **21**, 17265, doi: 10.1039/c1jm13374h.

[5] F. G. Córdova, Y. A. Ismail, J. G. Martinez, A. S. Al Harrasi, T. F. Otero, Electroactive Polymer Actuators and Devices (EAPAD) 2013, *SPIE*, 2013, 29-43, doi: 10.1117/12.2009609.

[6] N. Shoaie, M. Daneshpour, M. Azimzadeh, S. Mahshid, S. M. Khoshfetrat, F. Jahanpeyma, A. Gholaminejad, K. Omidfar, M. Foruzandeh, Electrochemical sensors and biosensors based on the use of polyaniline and its nanocomposites: a review on recent advances, *Microchimica Acta*, 2019, **186**, 465, doi: 10.1007/s00604-019-3588-1.

[7] J. Huang, S. Virji, B. H. Weiller, R. B. Kaner, Nanostructured polyaniline sensors, *Chemistry - A European Journal*, 2004, **10**, 1314-1319, doi: 10.1002/chem.200305211.

[8] J. Gao, A. J. Heeger, J. Y. Lee, C. Y. Kim, Soluble polypyrrole as the transparent anode in polymer light-emitting diodes, *Synthetic Metals*, 1996, **82**, 221-223, doi: 10.1016/s0379-6779(96)03794-0.

[9] Y. Yang, A. J. Heeger, Polyaniline as a transparent electrode for polymer light-emitting diodes: lower operating voltage and higher efficiency, *Applied Physics Letters*, 1994, **64**, 1245-1247, doi: 10.1063/1.110853.

[10] H. L. Wang, A. G. MacDiarmid, Y. Z. Wang, D. D. Gebier, A. J. Epstein, Application of polyaniline (emeraldine base, EB) in polymer light-emitting devices, *Synthetic Metals*, 1996, **78**, 33-37, doi: 10.1016/0379-6779(95)03569-6.

[11] P. Novák, K. Müller, K. S. V. Santhanam, O. Haas, Electrochemically active polymers for rechargeable batteries, *Chemical Reviews*, 1997, **97**, 207-282, doi: 10.1021/cr941181o.

[12] Y. Luo, R. Guo, T. Li, F. Li, Z. Liu, M. Zheng, B. Wang, Z. Yang, H. Luo, Y. Wan, Application of polyaniline for Li-ion batteries, lithium-sulfur batteries, and supercapacitors, *ChemSusChem*, 2019, **12**, 1591-1611, doi: 10.1002/cssc.201802186.

[13] Inamuddin, Y. A. Ismail, ynthesis and characterization of electrically conducting poly-o-methoxyaniline Zr(1V) molybdate Cd(II) selective composite cation-exchanger, *Desalination*, 2010, **250**, 523-529, doi: 10.1016/j.desal.2008.06.033.

[14] R. T. Richardson, A. K. Wise, B. C. Thompson, B. O. Flynn, P. J. Atkinson, N. J. Fretwell, J. B. Fallon, G. G. Wallace, R. K. Shepherd, G. M. Clark, Polypyrrole-coated electrodes for the delivery of charge and neurotrophins to cochlear neurons, *Biomaterials*, 2009, **30**, 2614-2624, doi: 10.1016/j.biomaterials.2009.01.015.

[15] P. M. Beaujuge, J. R. Reynolds, Color control in π-conjugated organic polymers for use in electrochromic devices, *Chemical Reviews*, 2010, **110**, 268-320, doi: 10.1021/cr900129a.

[16] J. D. Stenger-Smith, Intrinsically electrically conducting polymers. Synthesis, characterization, and their applications, *Progress in Polymer Science*, 1998, **23**, 57-79, doi: 10.1016/s0079-6700(97)00024-5.

[17] T. F. Otero, Biomimetic conducting polymers: synthesis, materials, properties, functions, and devices, *Polymer Reviews*, 2013, **53**, 311-351, doi: 10.1080/15583724.2013.805772.

[18] T. F. Otero, S. Beaumont, The energy consumed by electrochemical molecular machines as self-sensor of the reaction conditions: origin of sensing nervous pulses and asymmetry in biological functions, *ChemElectroChem*, 2018, **5**, 3335-3347, doi: 10.1002/celc.201800905.

[19] L. Rajan, M. P. Sidheekha, A. Shabeeba, Y. A. Ismail, Conducting polymers as bio-mimetic multistep macromolecular sensors of working conditions: polyindole/polyvinyl alcohol hybrid film senses electrical and chemical working ambient, *Materials Chemistry Frontiers*, 2022, **6**, 1706-1718, doi: 10.1039/d2qm00322h.

[20] A. K. Shabeeba, M. M. Manikandan, M. P. Sidheekha, L. Rajan, Y. A. Ismail, Poly-o-toluidine coated polyvinyl alcohol film: reaction driven sensing capabilities, *Materials Today: Proceedings*, 2022, **51**, 2293-2299, doi: 10.1016/j.matpr.2021.11.403.

[21] M. P. Sidheekha, K. Nufaira, A. K. Shabeeba, L. Rajan, Y. A. Ismail, Characterization of polyanilines synthesized at different pH for electrochemical sensing and supercapacitor applications, *Materials Today: Proceedings*, 2022, **51**, 2286-2292, doi: 10.1016/j.matpr.2021.11.402.

[22] A. Shabeeba, Y. A. Ismail, Chitosan/polypyrrole hybrid film as multistep electrochemical sensor: sensing electrical, thermal and chemical working ambient, *Materials Research Bulletin*, 2022, **152**, 111817, doi: 10.1016/j.materresbull.2022.111817.

[23] M. P. Sidheekha, G. E. Rajendran, A. K. Shabeeba, Y. A. Ismail, Current sensing supercapacitor electrodes based on chitosan/poly-o-toluidine hydrogel composites, *Journal of Materials Research*, 2021, **36**, 1914-1926, doi: 10.1557/s43578-021-00241-2.

[24] T. F. Otero, J. G. Martinez, Physical and chemical awareness from sensing polymeric artificial muscles, *Experiments and modeling, Progress in Polymer Science*, 2015, **44**, 62-78, doi: 10.1016/j.progpolymsci.2014.09.002.

[25] T. F. Otero, Reactions drive conformations. Biomimetic properties and devices, theoretical description, *Journal of Materials Chemistry B*, 2013, **1**, 3754-3767, doi: 10.1039/C3TB20112K.

[26] J. G. Martinez, T. F. Otero, Biomimetic dual sensing-actuators: theoretical description. sensing electrolyte concentration and driving current, *The Journal of Physical Chemistry B*, 2012, **116**, 9223-9230, doi: 10.1021/jp302931k.

[27] T. F. Otero, J. J. Sanchez, J. G. Martinez, Biomimetic dual

sensing-actuators based on conducting polymers. galvanostatic theoretical model for actuators sensing temperature, *The Journal of Physical Chemistry B*, 2012, **116**, 5279-5290, doi: 10.1021/jp300290s.

[28] Y. A. Ismail, J. Chang, S. R. Shin, R. S. Mane, S.-H. Han, S. J. Kim, Hydrogel-assisted polyaniline microfiber as controllable electrochemical actuatable supercapacitor, *Journal of the Electrochemical Society*, 2009, **156**, A313, doi: 10.1149/1.3077597.

[29] Q. B. Le, R. Kiefer, T. T. Dao, N. E. Kazantseva, P. Saha, Recent and future research related to the use of conducting polymers for supercapacitors, Springer, 2022, 289-309, doi: 10.1007/978-3-030-98021-4_16.

[30] M. Jaymand, Recent progress in chemical modification of polyaniline, *Progress in Polymer Science*, 2013, **38**, 1287-1306, doi: 10.1016/j.progpolymsci.2013.05.015.

[31] Y. A. Ismail, A. Ahmad, F. Mohammad, Synthesis, electrical, electronic and charge transport properties of poly(aniline-co-p-toluidine), *Journal of Macromolecular Science, Part A*, 2008, **45**, 650-657, doi: 10.1080/10601320802168868.

[32] A. I. Yahya, A. Ahmad, F. Mohammad, Electrical, electronic and thermal studies on poly[(aniline)co(*p*-methoxyanlline)] and poly [(*o*-toluidine)co(*p*-methoxyaniline)], *Indian Journal of Chemistry Section a*, 2004, 43A, 1423-1427.

[33] H. Ahmad, M. A. Ali, M. M. Rahman, M. A. Alam, K. Tauer, H. Minami, R. Shabnam, Novel carboxyl functional spherical electromagnetic polypyrrole nanocomposite polymer particles with good magnetic and conducting properties, *Polymer International*, 2016, **65**, 1179-1186, doi: 10.1002/pi.5169.

[34] K. S. Alva, J. Kumar, K. A. Marx, S. K. Tripathy, Enzymatic synthesis and characterization of a novel water-soluble polyaniline: poly(2, 5-diaminobenzenesulfonate), *Macromolecules*, 1997, **30**, 4024-4029, doi: 10.1021/ma961544h.

[35] G. Liao, Q. Li, Z. Xu, The chemical modification of polyaniline with enhanced properties: A review, *Progress in Organic Coatings*, 2019, **126**, 35-43, doi: 10.1016/j.porgcoat.2018.10.018.

[36] Y. A. Ismail, A. Shabeeba, M. P. Sidheekha, L. Rajan, in Actuators: Fundamentals, Principles, Materials and Applications, Ed. R. Inamuddin, A. M. Boddula, Asiri, John Wiley & Sons, Inc., Hoboken and Scrivener Publishing LLC, Beverly, 2020, 211-252.

[37] J. Bhadra, A. Alkareem, N. Al-Thani, A review of advances in the preparation and application of polyaniline based thermoset blends and composites, *Journal of Polymer Research*, 2020, **27**, 1-20, doi:10.1007/s10965-020-02052-1.

[38] R. Rajamany, S. Prakash, Y. A. Ismail, Synthesis and characterisation of polyaniline/polyvinyl alcohol composites as supercapacitor electrode materials, *Plastics, Rubber and Composites*, 2022, **51**, 240-249, doi: 10.1080/14658011.2021.1981090.

[39] E. N. Zare, P. Makvandi, B. Ashtari, F. Rossi, A. Motahari, G. Perale, Progress in conductive polyaniline-based nanocomposites for biomedical applications: a review, *Journal of Medicinal Chemistry*, 2020, **63**, 1-22, doi: 10.1021/acs.jmedchem.9b00803.

[40] C. Oueiny, S. Berlioz, F.-X. Perrin, Carbon nanotube-polyaniline composites, *Progress in Polymer Science*, 2014, **39**, 707-748, doi: 10.1016/j.progpolymsci.2013.08.009.

[41] S. Xing, G. Zhao, Morphology, structure, and conductivity of polypyrrole prepared in the presence of mixed surfactants in aqueous solutions, *Journal of Applied Polymer Science*, 2007, **104**, 1987-1996, doi: 10.1002/app.25912.

[42] X. Li, W. Zhao, R. Yin, X. Huang, L. Qian, A Highly Porous Polyaniline-Graphene Composite Used for Electrochemical Supercapacitors, *Engineered Science*, 2018, **3**, 89-95, doi: 10.30919/es8d743.

[43] A. Sajedi-Moghaddam, C. C. Mayorga-Martinez, E. Saievar-Iranizad, Z. Sofer, M. Pumera, Exfoliated transition metal dichalcogenide (MX_2; M = Mo, W; X = S, Se, Te) nanosheets and their composites with polyaniline nanofibers for electrochemical capacitors, *Applied Materials Today*, 2019, **16**, 280-289, doi: 10.1016/j.apmt.2019.06.002.

[44] S. ur Rehman, R. Ahmed, K. Ma, S. Xu, T. Tao, M.A. Aslam, M. Amir, J. Wang, Composite of strip-shaped zif-67 with polypyrrole: a conductive polymer-mof electrode system for stable and high specific capacitance, *Engineered Science*, 2020, **13**, 71-78, doi: 10.30919/es8d1263.

[45] Y. A. Ismail, J. G. Martínez, A. S. Al Harrasi, S. J. Kim, T. F. Otero, Sensing characteristics of a conducting polymer/hydrogel hybrid microfiber artificial muscle, *Sensors and Actuators B: Chemical*, 2011, **160**, 1180-1190, doi: 10.1016/j.snb.2011.09.044.

[46] Y. A. Ismail, J. G. Martínez, T. F. Otero, Fibroin/Polyaniline microfibrous mat. Preparation and electrochemical characterization as reactive sensor, *Electrochimica Acta*, 2014, **123**, 501-510, doi: 10.1016/j.electacta.2014.01.073.

[47] Y. A. Ismail, J. G. Martinez, T. F. Otero, Polyurethane microfibrous mat templated polypyrrole: preparation and biomimetic reactive sensing capabilities, *Journal of Electroanalytical Chemistry*, 2014, **719**, 47-53, doi: 10.1016/j.jelechem.2014.01.025.

[48] X. Wang, X. Zeng, D. Cao, Biomass-derived nitrogen-doped porous carbons (npc) and npc/ polyaniline composites as high-performance supercapacitor materials, *Engineered Science*, 2018, **1**, 55-63, doi: 10.30919/es.180325.

[49] V. Elayappan, V. Murugadoss, Z. Fei, P. J. Dyson, S. Angaiah, Influence of polypyrrole incorporated electrospun poly(vinylidene fluoride-co-hexafluoropropylene) nanofibrous composite membrane electrolyte on the photovoltaic performance of dye sensitized solar cell, *Engineered Science*, 2020, **10**, 78-84, doi: 10.30919/es5e1007.

[50] Q. Mu, R. Liu, H. Kimura, J. Li, H. Jiang, X. Zhang, Z. Yu, X. Sun, H. Algadi, Z. Guo, W. Du, C. Hou, Supramolecular self-assembly synthesis of hemoglobin-like amorphous CoP@N, P-doped carbon composites enable ultralong stable cycling under high-current density for lithium-ion battery anodes, *Advanced Composites and Hybrid Materials*, 2023, **6**, 23, doi: 10.1007/s42114-022-00607-y.

[51] Y. Wang, D. Yang, M. M. Hessien, K. Du, M. M. Ibrahim, Y. Su, G. A. M. Mersal, R. Ma, S. M. El-Bahy, M. Huang, Q. Yuan, B. Cui, D. Hu, Flexible Barium

titanate@polydopamine/polyvinylidene fluoride/polymethyl methacrylate nanocomposite films with high performance energy storage, *Advanced Composites and Hybrid Materials*, 2022, **5**, 2106-2115, doi: 10.1007/s42114-022-00552-w.

[25] P. Wang, T. Song, H. M. Abo-Dief, J. Song, A. K. Alanazi, B. Fan, M. Huang, Z. Lin, A. A. Altalhi, S. Gao, L. Yang, J. Liu, S. Feng, T. Cao, Effect of carbon nanotubes on the interface evolution and dielectric properties of polylactic acid/ethylene-vinyl acetate copolymer nanocomposites, *Advanced Composites and Hybrid Materials*, 2022, **5**, 1100-1110, doi: 10.1007/s42114-022-00489-0.

[53] W. Yang, D. Peng, H. Kimura, X. Zhang, X. Sun, R. A. Pashameah, E. Alzahrani, B. Wang, Z. Guo, W. Du, C. Hou, Honeycomb-like nitrogen-doped porous carbon decorated with Co_3O_4 nanoparticles for superior electrochemical performance pseudo-capacitive lithium storage and supercapacitors, *Advanced Composites and Hybrid Materials*, 2022, **5**, 3146-3157, doi: 10.1007/s42114-022-00556-6.

[54] H. Li, Y. Fu, D. Alhashmialameer, H. K. Thabet, P. Zhang, C. Wang, K. Zhu, M. Huang, Z. Guo, F. Dang, Lattice distortion embedded core-shell nanoparticle through epitaxial growth Barium titanate shell on the strontium titanate core with enhanced dielectric response, *Advanced Composites and Hybrid Materials*, 2022, **5**, 2631-2641, doi: 10.1007/s42114-022-00548-6.

[55] C. Lai, Y. Guo, H. Zhao, H. Song, X. Qu, M. Huang, S. W. Hong, K. Lee, High-performance double "ion-buffering reservoirs of asymmetric supercapacitors enabled by battery-type hierarchical porous sandwich-like Co_3O_4 and 3D graphene aerogels, *Advanced Composites and Hybrid Materials*, 2022, **5**, 2557-2574, doi: 10.1007/s42114-022-00532-0.

[56] T. Gao, H. Rong, K. H. Mahmoud, J. Ruan, S. M. El-Bahy, A. A. Faheim, Y. Li, M. Huang, M. A. Nassan, R. Zhao, Iron/silicon carbide composites with tunable high-frequency magnetic and dielectric properties for potential electromagnetic wave absorption, *Advanced Composites and Hybrid Materials*, 2022, **5**, 1158-1167, doi: 10.1007/s42114-022-00507-1.

[57] W. Shao, R. Jamal, F. Xu, A. Ubul, T. Abdiryim, The effect of a small amount of water on the structure and electrochemical properties of solid-state synthesized polyaniline, *Materials*, 2012, **5**, 1811-1825, doi: 10.3390/ma5101811.

[58] P. Kong, H. Feng, N. Chen, Y. Lu, S. Li, P. Wang, Polyaniline/chitosan as a corrosion inhibitor for mild steel in acidic medium, *RSC Advances*, 2019, **9**, 9211-9217, doi: 10.1039/c9ra00029a.

[59] C. Qu, P. Zhao, Y. Ren, C. Wu, J. Liu, Increase the surface PANI occupancy of electrospun PMMA/PANI fibers: effect of the electrospinning parameters on surface segregation, *Polymers*, 2022, **14**, 3401, doi: 10.3390/polym14163401.

[60] F. Usman, J. O. Dennis, K. C. Seong, A. Yousif Ahmed, F. Meriaudeau, O. B. Ayodele, A. R. Tobi, A. Abdelkarim S Rabih, A. Yar, Synthesis and characterisation of a ternary composite of polyaniline, reduced graphene-oxide and chitosan with reduced optical band gap and stable aqueous dispersibility, *Results in Physics*, 2019, **15**, 102690, doi: 10.1016/j.rinp.2019.102690.

[61] Y. A. Ismail, S. R. Shin, K. M. Shin, S. G. Yoon, K. Shon, S. I. Kim, S. J. Kim, Electrochemical actuation in chitosan/polyaniline microfibers for artificial muscles fabricated using an in situ polymerization, *Sensors and Actuators B: Chemical*, 2008, **129**, 834-840, doi: 10.1016/j.snb.2007.09.083.

[62] T. F. Otero, Coulovoltammetric and dynamovoltammetric responses from conducting polymers and bilayer muscles as tools to identify reaction-driven structural changes. A review, *Electrochimica Acta*, 2016, **212**, 440-457, doi: 10.1016/j.electacta.2016.07.004.

[63] T. F. Otero, M. Alfaro, V. Martinez, M. A. Perez, J. G. Martinez, Biomimetic structural electrochemistry from conducting polymers: processes, charges, and energies. coulovoltammetric results from films on metals revisited, *Advanced Functional Materials*, 2013, **23**, 3929-3940, doi: 10.1002/adfm.201203502.

[64] T. F. Otero, Conducting polymers, electrochemistry, and biomimicking processes. Modern Aspects of Electrochemistry. Boston: Kluwer Academic Publishers, 2005, 307-434, doi: 10.1007/0-306-46917-0_3.

[65] T. F. Otero, J. G. Martinez, J. Arias-Pardilla, Biomimetic electrochemistry from conducting polymers. A review, Electrochimica Acta, 2012, **84**, 112-128, doi: 10.1016/j.electacta.2012.03.097.

[66] T. F. Otero, J. G. Martinez, Biomimetic intracellular matrix (ICM) materials, properties and functions. Full integration of actuators and sensors, *Journal of Material Chemistry B*, 2013, **1**, 26-38, doi: 10.1039/c2tb00176d.

[67] F. Xu, G. Zheng, D. Wu, Y. Liang, Z. Li, R. Fu, Improving electrochemical performance of polyaniline by introducing carbon aerogel as filler, *Physical Chemistry Chemical Physics*, 2010, **12**, 3270, doi: 10.1039/b917677b.

[68] W. Li, F. Gao, X. Wang, N. Zhang, M. Ma, Strong and robust polyaniline-based supramolecular hydrogels for flexible supercapacitors, *Angewandte Chemie*, 2016, **128**, 9342-9347, doi: 10.1002/ange.201603417.

[69] M. Zhang, A. Nautiyal, H. Du, Z. Wei, X. Zhang, R. Wang, Electropolymerization of polyaniline as high-performance binder free electrodes for flexible supercapacitor, *Electrochimica Acta*, 2021, **376**, 138037, doi: 10.1016/j.electacta.2021.138037.

[70] M. Z. Iqbal, M. M. Faisal, M. Sulman, S. R. Ali, A. M. Afzal, M. A. Kamran, T. Alharbi, Capacitive and diffusive contribution in strontium phosphide-polyaniline based supercapattery, *Journal of Energy Storage*, 2020, **29**, 101324, doi: 10.1016/j.est.2020.101324.

[71] X. Zang, X. Li, M. Zhu, X. Li, Z. Zhen, Y. He, K. Wang, J. Wei, F. Kang, H. Zhu, Graphene/polyaniline woven fabric composite films as flexible supercapacitor electrodes, *Nanoscale*, 2015, **7**, 7318-7322, doi: 10.1039/c5nr00584a.

[72] J. Yang, X. Yu, X. Sun, Q. Kang, L. Zhu, G. Qin, A. Zhou, G. Sun, Q. Chen, Polyaniline-decorated supramolecular hydrogel with tough, fatigue-resistant, and self-healable performances for all-In-one flexible supercapacitors, *ACS Applied Materials & Interfaces*, 2020, **12**, 9736-9745, doi: 10.1021/acsami.9b20573.

[73] Z. Liu, J. Chen, Y. Zhan, B. Liu, C. Xiong, Q. Yang, G.-H. Hu, Fe^{3+} cross-linked polyaniline/cellulose nanofibril hydrogels

for high-performance flexible solid-state supercapacitors, *ACS Sustainable Chemistry & Engineering*, 2019, **7**, 17653-17660, doi: 10.1021/acssuschemeng.9b03674.

[74] R. Jia, H. Du, X. Zhang, Z. Chen, D. Chen, Stretchable and compressible supercapacitor with polyaniline on hydrogel electrolyte, *Journal of The Electrochemical Society*, 2018, **165**, A3792, doi: 10.1149/2.0481816jes.

[75] Y. Fu, H. Wu, S. Ye, X. Cai, X. Yu, S. Hou, H. Kafafy, D. Zou, Integrated power fiber for energy conversion and storage, *Energy & Environmental Science*, 2013, **6**, 805, doi: 10.1039/c3ee23970e.

[76] G. Li, L. Wang, X. Lei, Z. Peng, T. Wan, S. Maganti, M. Huang, V. Murugadoss, I. Seok, Q. Jiang, D. Cui, A. Alhadhrami, M. M. Ibrahim, H. Wei, Flexible, yet robust polyaniline coated foamed polylactic acid composite electrodes for high-performance supercapacitors, *Advanced Composites and Hybrid Materials*, 2022, **6**, 1-11, doi: 10.1007/s42114-022-00501-7.

[77] S. H. Park, J.-M. Jeong, S. J. Kim, K. H. Kim, S. H. Lee, N. H. Bae, K. G. Lee, B. G. Choi, Large-area and 3D polyaniline nanoweb film for flexible supercapacitors with high rate capability and long cycle life, *ACS Applied Energy Materials*, 2020, **3**, 7746-7755, doi: 10.1021/acsaem.0c01140.

[78] L. Li, J. Zhang, Z. Peng, Y. Li, C. Gao, Y. Ji, R. Ye, N. Dong Kim, Q. Zhong, Y. Yang, H. Fei, G. Ruan, J. M. Tour, High-performance pseudocapacitive microsupercapacitors from laser-induced graphene, *Advanced Materials*, 2016, **28**, 838-845, doi: 10.1002/adma.201503333.